

# One World, Dual Timeline: Decoupled Spatio-Temporal Gaussian Scene Graph for 4D Cooperative Driving Reconstruction

Yulong Chen<sup>▲♣\*</sup>, Xiaoyun Dong<sup>♣\*</sup>, Haoyu Zhang<sup>♣♣\*</sup>, Zongxian Yang<sup>♣</sup>, Lewei Xie<sup>▲</sup>,  
Xinke Li<sup>♣†</sup>, Yifan Zhang<sup>♣†</sup>, Kai Wang<sup>♣†</sup>, Jianping Wang<sup>♣</sup>

<sup>▲</sup> City University of Hong Kong (Dongguan), Guangdong, China

<sup>♣</sup> City University of Hong Kong, Hong Kong, China

<sup>♣♣</sup> SLAI, Shenzhen, China

72405526@cityu-dg.edu.cn xiaodong8@cityu.edu.hk hzhang2838-c@my.cityu.edu.hk

zongxian.yang@cityu-dg.edu.cn 72404204@cityu-dg.edu.cn xinkeli@cityu.edu.hk

kai.wang@cityu-dg.edu.cn yifan.zhang@cityu-dg.edu.cn jianwang@cityu.edu.hk

## Abstract

Reconstructing dynamic scenes from Vehicle-to-Infrastructure Cooperative Autonomous Driving (VICAD) data is fundamentally complicated by temporal asynchrony: vehicle and infrastructure cameras operate on independent clocks, capturing the same dynamic agent such as cars and pedestrians at different physical times. Existing Gaussian Scene Graph methods implicitly assume synchronized observations and assign a single pose per agent per frame, which is an assumption that breaks in cooperative settings, where the resulting gradient conflicts cause severe ghosting on dynamic agents. We identify this as a *representation-level failure*, not an optimization artifact: we prove that any single-timeline formulation incurs an irreducible photometric loss scaling quadratically with agent velocity and cross-source time offset. To resolve this, we propose **DUST** (**Deco**Upled **S**patio-**T**emporal) Gaussian Scene Graph for 4D Cooperative Driving Reconstruction. DUST Gaussian scene graph shares a canonical Gaussian set per agent for appearance consistency, while maintaining decouple pose trajectories aligned to each source’s true capture timestamps. We prove that this decoupling enables the pose-gradient kernel block-diagonal, eliminating cross-source interference entirely. To make DUST practical, we further introduce a static anchor-based pose correction pipeline that corrects spatio misalignment between vehicle and infrastructure annotations, and a pose-regularized joint optimization scheme that prevents trajectory jitter and drift during early training. On 26 sequences from V2X-Seq, DUST achieves state-of-the-art performance, improving dynamic-area PSNR by 3.2 dB over the strongest baseline and reducing Fréchet Video Distance by 37.7%, with keeping robustness under larger temporal asynchrony.

## 1 Introduction

High-fidelity 4D scene reconstruction [3, 7, 26, 34] has become a practical alternative to real-world data collection for autonomous driving: it converts recorded driving logs into photorealistic digital environments that support novel-view synthesis (NVS), scene editing, and scalable simulation. A particularly compelling use case arises in Vehicle-to-Infrastructure Cooperative Autonomous

\*Indicates equal contribution.

†Corresponding authors.

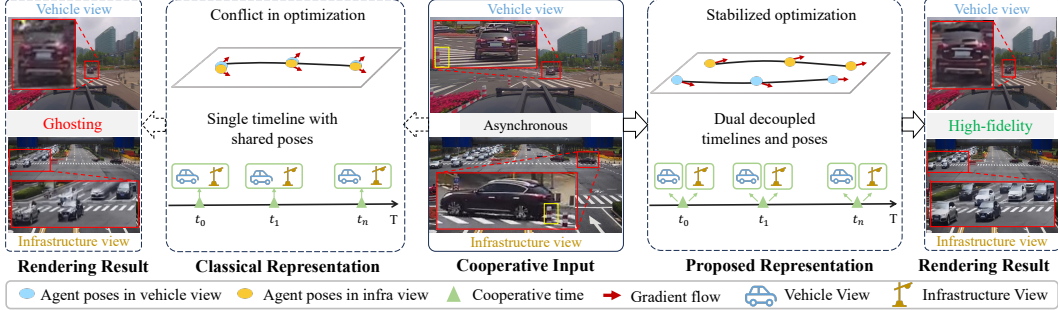


Figure 1: **Comparison of scene representations. Cooperative Input:** Vehicle and infrastructure sensors capture dynamic scenes asynchronously. **Top:** the black car has passed the pole; **Bottom:** it has not. **Classical Representation:** Aligning these asynchronous observations to one timeline creates conflicting gradients, leading to severe ghosting. **Proposed Representation:** Our DUST-GSG assigns separate pose timelines to each source while sharing canonical Gaussians, which removes gradient conflicts and enables stable, high-fidelity reconstruction.

Driving (VICAD) [11, 15, 25, 28, 32], where both a moving vehicle and fixed roadside cameras (i.e., infrastructure) observe the same scene. Reconstructing from both sources jointly enables observations that neither platform can produce alone, while also alleviating the shortage of real paired vehicle-infrastructure data, which is costly to collect at scale.

Recent driving reconstruction methods [3, 26, 34] commonly adopt the Gaussian Scene Graph (GSG) to decompose a scene into a static background and dynamic agents, achieving strong results on single-platform data. These formulations all rest on an implicit assumption: at each frame, all observations share one timeline, and each dynamic agent is described by a single pose. This holds when sensors are driven by a common clock, but breaks down in cooperative settings, where vehicle and infrastructure cameras are triggered independently and their observations are inherently asynchronous. Forcing such asynchronous observations to share one pose induces conflicting gradients during optimization and produces ghosting on dynamic agents (Fig. 1). A concurrent effort on cooperative reconstruction [22] does not address this temporal asynchrony. The core challenge is therefore *how to faithfully represent asynchronous multi-source observations in a unified 4D scene*.

We propose **DUST**, a 4D cooperative reconstruction framework based on a Decoupled Spatio-Temporal Gaussian Scene Graph (DUST-GSG). DUST-GSG models each dynamic agent with a shared set of canonical Gaussians to ensure appearance consistency, while assigning separate pose timelines to the vehicle and infrastructure sources (Fig. 2). This decoupled design allows each source to render from its exact timestamp, directly eliminating the gradient conflicts caused by asynchronous observations. We further provide *theoretical analysis* demonstrating that forcing a single timeline inherently causes reconstruction errors, whereas DUST-GSG mathematically resolves it. Beyond this theoretical design, applying our DUST-GSG to real cooperative data requires overcoming two problems. First, raw cooperative labels often contain spatio misalignment and provide poor pose initialization for DUST-GSG. We resolve this through a pose correction method. We use static vehicles as anchors to align labels from two sources, then regenerate cooperative labels for accurate initialization. Second, during reconstruction training, optimizing poses from pure image supervision easily leads to temporal drift and jitter. We address this by introducing a joint optimization scheme with pose regularization. This scheme enforces smooth motion across frames and prevents the poses from drifting away from their initial states. Combined with these two designs, DUST ensures robust and high-fidelity cooperative reconstruction under asynchronous conditions.

Our main contributions are as follows:

- We propose DUST, a cooperative reconstruction paradigm using a Decoupled Spatio-Temporal Gaussian Scene Graph. We also provide a theoretical analysis of this paradigm.
- We introduce a static anchor-based pose correction pipeline to refine vehicle-infrastructure alignment, subsequently regenerating cooperative labels offline to initialize agent poses.
- We propose a pose-regularized joint optimization scheme for Gaussian parameters and agent poses, which enforces smooth 3D motion and effectively mitigates early-stage drift.

- Evaluated on the V2X-Seq, DUST achieves state-of-the-art performance in scene reconstruction and NVS, significantly outperforming previous methods in terms of dynamic area metrics (+3.2 dB PSNR and -37.7% FVD) for reconstruction.

## 2 Related Work

**4D Driving Scene Reconstruction.** Recent driving reconstruction methods [1, 4, 5, 7, 10, 13, 20] build upon NeRF and 3D Gaussian Splatting to model dynamic urban environments. A dominant paradigm decomposes the scene into static backgrounds and dynamic agents. OMNIRE[3], StreetGS[26], and DrivingGaussian[34] track vehicles using explicit 3D tracking boxes and render them from canonical spaces. Other approaches like PVG[2] avoid tracking boxes to model general scene vibrations. Extending these representations to cooperative reconstruction is an emerging frontier. For example, CRUISE [22] explores generative scene editing for cooperative scenarios. However, all these existing frameworks rely on a single timeline constraint. They assume perfectly synchronized cameras across all observations. In real cooperative driving systems, vehicle and infrastructure sensors operate on independent hardware clocks. This hardware independence creates natural time gaps between cross observations. When existing methods force these asynchronous inputs into a single shared timeline, they inevitably produce severe artifacts. Our work directly targets this fundamental system limitation.

**Vehicle-Infrastructure Cooperative Autonomous Driving.** Cooperative systems share sensor data across vehicles and infrastructure to overcome physical line of sight limitations. Methods like DiscoNet [9] and V2X-ViT [23] exchange deep features to improve object detection. Other works optimize communication bandwidth [6] or address spatial misalignment [12]. However, developing and evaluating these algorithms requires massive amounts of driving data. Most existing models are trained on purely synthetic datasets [21, 23]. These virtual environments fail to capture natural sensor data and complex physical constraints. While datasets like DAIR-V2X [30] and V2X-Seq [31] solve this by providing real world observations, datasets cannot simulate new behaviors. Therefore, the cooperative autonomous driving industry urgently needs highly realistic simulation environments for algorithm development and testing. Our framework transforms real sequential data into fully controllable digital twins to directly serve this exact purpose.

## 3 Method

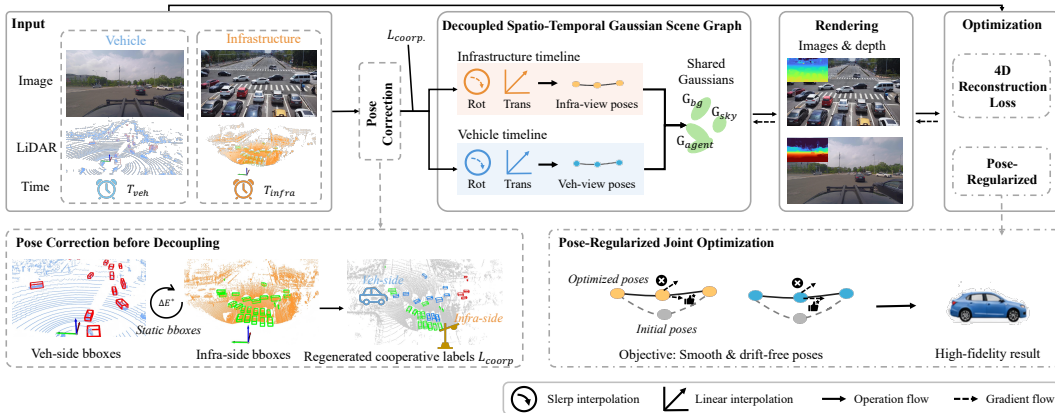


Figure 2: **Overview of DUST.** DUST first regenerates cooperative labels offline using co-visible static vehicles as anchors. The pose correction initialize a Decoupled Spatio-Temporal Gaussian Scene Graph, where each dynamic agent shares canonical Gaussians but maintains separate vehicle-side and infrastructure-side pose timelines. Joint optimization then refines Gaussian parameters and dual-timeline poses with pose regularization for stable cooperative reconstruction.

Our proposed DUST framework uses inputs from both the vehicle and the infrastructure, including image sequences, camera poses, and cooperative tracking bounding boxes. Our goal is to learn a shared 4D Gaussian scene representation supervised by data from both sources. This directly supports novel view synthesis, scene editing, and driving simulation. First, Sec.3.1 introduces the Decoupled Spatio-Temporal Gaussian Scene Graph (DUST-GSG). Next, Sec.3.2 theoretically proves

that DUST-GSG resolves the reconstruction errors caused by single-timeline modeling. Finally, to make DUST-GSG practical, Sec.3.3 further introduces a pose correction step for accurate DUST-GSG initialization, and a joint optimization scheme that stabilizes the overall training process.

### 3.1 Decoupled spatio-Temporal Gaussian Scene Graph

**Gaussian Scene Graph.** The Gaussian Scene Graph (GSG) [3, 26, 34] organizes a driving scene into a structured graph of 3D Gaussian nodes, enabling joint reconstruction of static environments and dynamic agents. It decomposes the scene into a time-invariant background node  $\mathcal{V}_{bg}$ , a sky node  $\mathcal{V}_{sky}$ , and a set of dynamic agent nodes  $\{\mathcal{V}_{ag}\}$  for moving objects such as vehicles and pedestrians, where each node is represented as a set of 3D Gaussian primitives  $\mathcal{G}$ . The background and sky nodes are static and time-invariant. The dynamic agents are further classified into rigid agents, such as cars and trucks, and non-rigid agents, like pedestrians and cyclists. For these agents, the key insight is to represent each agent by a *canonical* Gaussian set  $G_{ag} = \{\mathcal{G}_n\}_{n=1}^N$ , a fixed appearance defined in the agent’s local frame, decoupled from a pose trajectory  $T(t) \in SE(3)$  that places the agent in the world at time  $t$ :

$$\mathcal{V}_{ag}(t) = T(t) \otimes f_t(G_{ag}). \quad (1)$$

Here,  $f_t : \mathbb{G} \rightarrow \mathbb{G}$  models the internal shape deformation of the agent, and  $\mathbb{G} = \bigcup_{N \in \mathbb{N}} \{\{\mathcal{G}_n\}_{n=1}^N\}$  denotes the space of 3D Gaussian sets. For rigid agents,  $f_t$  is simply the identity mapping. For non-rigid agents,  $f_t$  serves as a time-dependent deformation field [29] that captures local movements like limb motion. This factorization of a shared canonical shape optimized across all frames and a per-frame pose learned from image supervision makes GSG efficient and expressive for single-vehicle driving reconstruction.

**Limitation in VICAD.** In VICAD, however, vehicle and infrastructure cameras are triggered asynchronously: each source  $c \in \{\text{veh}, \text{infra}\}$  captures the same agent at a different physical time  $t_i^c \neq t_i$ . For static elements this discrepancy is negligible, but dynamic agents physically occupy different world positions at  $t_i^{\text{veh}}$  and  $t_i^{\text{infra}}$ . Forcing both sources to share a single pose  $T(t_i)$  thus attributes contradictory image gradients to the same Gaussian primitives, causing the canonical shape to receive conflicting supervision and the reconstructed geometry to be systematically misaligned.

**Decoupled spatio-Temporal Gaussian Scene Graph (DUST-GSG).** To address this, DUST-GSG keeps the canonical Gaussians  $G_{ag}$  and deformation field  $f_t$  *shared* across both sources for spatio consistency, but *splits* the pose trajectory into two source-specific sequences  $\{T^{\text{veh}}(t_i^{\text{veh}})\}$  and  $\{T^{\text{infra}}(t_i^{\text{infra}})\}$  aligned to each source’s true capture times. The pose trajectory is initialized from cooperative labels. These labels include all visible agents from both observations. For each agent, the labels provide a sequence of 3D bounding boxes that track its position and orientation over time. To obtain the initial pose  $T^c(t_i^c)$  for a specific source  $c$  at query time  $t_i^c$ , we interpolate between these bounding boxes. We compute the position using linear interpolation and the rotation using spherical linear interpolation (Slerp [16]). Each dynamic agent node is defined as a triplet:

$$\mathcal{V}_{ag}^{\text{DST}} := \left\{ G_{ag}, \{T^{\text{veh}}(t_i^{\text{veh}})\}_{i=0}^{K-1}, \{T^{\text{infra}}(t_i^{\text{infra}})\}_{i=0}^{K-1} \right\}, \quad (2)$$

At render time, source  $c$  queries its own trajectory at its own capture time  $t_i^c$ :

$$\mathcal{V}_{ag}^c(t_i^c) = T^c(t_i^c) \otimes f_{t_i^c}(G_{ag}), \quad c \in \{\text{veh}, \text{infra}\}. \quad (3)$$

This factorization of a shared canonical shape and source-specific pose trajectories forms the foundation of our DUST-GSG. Following OMNIRE [3], we optimize all Gaussian parameters via differentiable rendering, but extend the optimization to jointly supervise the shared canonical Gaussians  $G_{ag}$  using image observations from both the vehicle and infrastructure sources.

### 3.2 Theoretical Justification of DUST-GSG

Single-timeline methods fail in VICAD reconstruction because asynchronous sources observe the same agent at different physical times. Let  $\Delta\tau = t_i^{\text{veh}} - t_i^{\text{infra}}$  be the capture-time offset at cooperative timestamp  $t_i$ . We formalize this failure and its remedy below; full proofs are in Appendix B.

**Theorem 1.** *Consider a dynamic agent with canonical Gaussians  $G_{ag} = \{\mathcal{G}_n\}_{n=1}^N$  (Eq. (1)) moving at velocity  $v \in \mathbb{R}^3$  during offset  $\Delta\tau$ . Let  $\mathcal{L}$  be the total photometric reconstruction loss over both sources. The following properties hold under local linearized rendering.*

**1. Irreducible Error of Single Timeline.** If both sources share a single pose  $T(t_i) \in SE(3)$ , the optimal loss satisfies

$$\mathcal{L}_{\text{single}}^* \geq \frac{|\Delta\tau|^2 \|\mathbf{v}\|^2}{4} \sum_{n=1}^N \lambda_n > 0, \quad (4)$$

where  $\lambda_n > 0$  is the minimum Fisher-information eigenvalue of  $\mathcal{G}_n$ , quantifying its photometric sensitivity to displacement.

**2. Decoupling Property of DUST-GSG.** Under  $\mathcal{V}_{\text{ag}}^{\text{DST}}$  with source-specific trajectories  $\{T^{\text{veh}}(t_i^{\text{veh}})\}$  and  $\{T^{\text{infra}}(t_i^{\text{infra}})\}$ , a zero-loss solution exists ( $\mathcal{L}_{\text{DST}}^* = 0$ ), and the two pose sequences optimize independently: a gradient update to  $\{T^{\text{veh}}\}$  induces no change in the infrastructure loss, and vice versa.

**Discussion.** ❶ Property 1 shows the failure is **representational**: no choice of  $G_{\text{ag}}$  can drive the loss to zero, and the irreducible error grows quadratically with both  $\|\mathbf{v}\|$  and  $|\Delta\tau|$ . For a vehicle at 10 m/s with  $|\Delta\tau| = 70$  ms, the implied misalignment reaches 0.7 m, well beyond the support radius of a single Gaussian, which directly causes the ghosting in Fig. 1. ❷ Property 2 shows DUST-GSG eliminates this at the representation level: source-specific poses absorb the temporal gap, so  $G_{\text{ag}}$  encodes only intrinsic geometry and both timelines converge without mutual interference. This motivates the pose correction and regularization strategies described in the following.

### 3.3 More Techniques for DUST-GSG

**Pose Correction before Decoupling.** Cooperative labels, i.e., bounding boxes, in dataset [30] merge vehicle and infrastructure annotations based on provided infrastructure-to-vehicle poses. However, small pose errors often cause noticeable misalignment between the two sources. Because DUST-GSG uses these labels to initialize the pose trajectories  $T^c(t_i^c)$ , inaccurate labels will degrade reconstruction quality. To address this, we introduce an offline pose correction step before decoupling.

At each cooperative timestamp  $t_i$ , let  $E_i \in SE(3)$  be the infrastructure-to-vehicle pose. We use co-visible static vehicles as geometric anchors to avoid dynamic interference. We match these static vehicles across both views using the Hungarian method [8], and let  $\mathcal{M}_i$  denote the set of matched vehicles at timestamp  $t_i$ . For a matched vehicle  $m \in \mathcal{M}_i$ , let  $\mathbf{X}_m^{\text{veh}}(t_i), \mathbf{X}_m^{\text{infra}}(t_i) \in \mathbb{R}^{8 \times 3}$  be the 3D bounding box corner matrices in the vehicle and infrastructure coordinates, respectively. We estimate a 6-DoF [35] pose correction  $\Delta E_i \in SE(3)$  by minimizing the corner alignment error:

$$\Delta E_i^* = \arg \min_{\Delta E_i \in SE(3)} \frac{1}{|\mathcal{M}_i|} \sum_{m \in \mathcal{M}_i} \|\mathbf{X}_m^{\text{veh}}(t_i) - \Delta E_i E_i \mathbf{X}_m^{\text{infra}}(t_i)\|_F^2. \quad (5)$$

We optimize this using L-BFGS [14]. Multiplying the optimal correction  $\Delta E_i^*$  by the original pose  $E_i$  gives the refined pose. For co-visible objects, we use this refined pose to project infrastructure annotations into the vehicle coordinate system to form cooperative annotation. Objects observed by only one source are kept after being transformed into the unified coordinate system.

Based on these regenerated labels, we interpolate poses to fill short missing segments in agent tracks. For an agent  $a$  missing a pose at time  $t_i$ , bounded by a preceding valid timestamp  $t_s$  and a subsequent valid timestamp  $t_e$ , we estimate the intermediate pose  $T_a(t_i)$ . We compute the translation via linear interpolation and the rotation via Slerp [16] between these two bounding poses. We only fill gaps of up to two frames. This procedure produces the pose correction for accurate DUST-GSG initialization.

**Pose-Regularized Joint Optimization.** DUST-GSG shares the canonical Gaussians of each dynamic agent across views while maintaining source-specific pose trajectories in dual timelines. Although pose correction provide a good initialization, directly optimizing poses using only image supervision causes drift and frame-to-frame jitter. We therefore introduce a pose regularization loss. Let  $T_a^c(t_i^c)$  be the initialized pose of agent  $a$  in source  $c \in \{\text{veh}, \text{infra}\}$ , and  $\tilde{T}_a^c(t_i^c)$  be its optimized pose.

First, we force the optimized 3D trajectory to be smooth over time. Specifically, an agent’s position at a given frame should closely match the linear interpolation of its past and future positions. For source  $c$  and timestamp  $t_i^c$ , let  $\mathcal{A}_i^c$  be the set of valid dynamic agents. We define the smoothness loss as:

$$\mathcal{L}_{\text{smooth}} = \frac{1}{|\mathcal{A}_i^c|} \sum_{a \in \mathcal{A}_i^c} \left\| \tilde{T}_a^c(t_i^c) - \left[ \tilde{T}_a^c(t_{i-1}^c) + w \left( \tilde{T}_a^c(t_{i+1}^c) - \tilde{T}_a^c(t_{i-1}^c) \right) \right] \right\|_2, \quad (6)$$

where  $w = \frac{t_i^c - t_{i-1}^c}{t_{i+1}^c - t_{i-1}^c}$ . Agents lacking valid past or future poses are excluded from  $\mathcal{A}_i^c$  for this calculation. This term is applied independently to both timelines.

Second, we constrain the optimized 3D positions to remain close to their initialized positions during early training:

$$\mathcal{L}_{\text{drift}} = \gamma(s) \frac{1}{|\mathcal{A}_i^c|} \sum_{a \in \mathcal{A}_i^c} \left\| \tilde{T}_a^c(t_i^c) - T_a^c(t_i^c) \right\|_2, \quad (7)$$

where  $s$  is the current training step. The weight  $\gamma(s)$  linearly decays to zero during training. This prevents poses from deviating before the Gaussian attributes become stable. As training proceeds, the constraint vanishes and image supervision naturally refines the poses.

The final training objective combines image rendering, geometric supervision, standard regularization, and the proposed pose regularization:

$$\mathcal{L} = \mathcal{L}_{\text{image}} + \lambda_{\text{depth}} \mathcal{L}_{\text{depth}} + \lambda_{\text{opacity}} \mathcal{L}_{\text{opacity}} + \mathcal{L}_{\text{reg}} + \lambda_{\text{smooth}} \mathcal{L}_{\text{smooth}} + \lambda_{\text{drift}} \mathcal{L}_{\text{drift}}. \quad (8)$$

Here,  $\mathcal{L}_{\text{image}}$  is the image reconstruction loss based on L1 and SSIM.  $\mathcal{L}_{\text{depth}}$  uses sparse LiDAR supervision from both vehicle and infrastructure sensors.  $\mathcal{L}_{\text{opacity}}$  regularizes the rendered opacity.  $\mathcal{L}_{\text{reg}}$  contains the standard Gaussian regularization terms [3]. Details are provided in the Appendix C.

## 4 Experiment

In this section, we benchmark the reconstruction capabilities of DUST against prior methods, focusing on dynamic scene reconstruction and novel view synthesis.

### 4.1 Experimental Setups

**Dataset.** We evaluate our method on 26 diverse sequences selected from the large-scale V2X-Seq dataset [31]. These sequences cover various times of day, weather and traffic densities [27, 24] (see Appendix D for the full list). All images are processed at their original resolution of  $1080 \times 1920$ . To ensure spatio consistency, we regenerate the cooperative annotations for all sequences.

**Evaluation.** Each cooperative timestamp provides a paired vehicle and infrastructure image. For scene reconstruction, we use all frames for both training and evaluation. For novel view synthesis, we hold out every 10th timestamp for testing, excluding both the vehicle and infrastructure images at these specific timestamps from the training set. We measure reconstruction quality using PSNR, SSIM, and LPIPS. Since dynamic objects represent the core challenge in asynchronous cooperative reconstruction, we specifically report these metrics on dynamic areas, masked using the provided 2D bounding boxes [31]. Furthermore, we report FVD [18] and RAFT-EPE [17] on these dynamic areas to evaluate temporal and motion consistency.

**Baselines.** We compare DUST against several Gaussian Splatting approaches: PVG [2], OMNIRE [3], 3DGS [7], CRUISE [22], StreetGS [26], and DeformableGS [29]. Among methods compared, for PVG, OMNIRE, StreetGS and DeformableGS, using their official implementations from the OMNIRE toolbox [3]. For a strictly fair comparison, all baselines are trained from scratch using the same data splits, evaluation protocols, and our regenerated annotations.

**Implementation Details.** We train all methods for 30,000 iterations per scene on a single NVIDIA A100 GPU. For DUST, the regularization coefficients are  $\lambda_{\text{smooth}} = 0.01$  and  $\lambda_{\text{drift}} = 0.01$ . During inference, our model achieves real-time rendering at  $\sim 20$  FPS at  $1080 \times 1920$  resolution.

Details on the datasets, metrics, baselines, and implementation can be found in Appendix C and D.

### 4.2 Main Results

As shown in Tab. 1, DUST achieves state-of-the-art performance in dynamic areas and full images. For instance, our dynamic PSNR in scene reconstruction exceeds the second-best PVG by 3.2 dB. Previous methods like OMNIRE and StreetGS force asynchronous observations into a single timeline. This shared-pose assumption creates optimization conflicts for dynamic agents. By decoupling the timelines, our DUST-GSG directly resolves these conflicts and recovers accurate appearances. Multi-frame metrics further confirm this advantage. DUST improves scene reconstruction FVD by

Table 1: **Performance comparison of scene reconstruction and NVS on the V2X-Seq dataset.** DUST outperforms prior Gaussian methods under all conditions, achieving substantial improvement in dynamic areas. CIs and Cond denote sequence categories and conditions. Full averages all 26 sequences. **Red** and **Blue** indicate the best and second-best results in a Cond line or Full line.

Method	Cls.	Cond.	Scene Reconstruction								Novel View Synthesis							
			Full Image				Dynamic Area				Full Image				Dynamic Area			
			PSNR↑	SSIM↑	LPIPS↓		PSNR↑	SSIM↑	FVD↓	EPE↓	PSNR↑	SSIM↑	LPIPS↓		PSNR↑	SSIM↑	FVD↓	EPE↓
3DGS [7] (2023)	Time	Noon	21.81	0.784	0.318	14.88	0.376	555.0	26.92	18.14	0.736	0.358	13.51	0.362	613.3	56.56		
		Dusk	22.10	0.809	0.310	14.03	0.336	465.3	25.84	17.92	0.755	0.358	12.30	0.311	1110.6	63.48		
	Weather	Normal	22.57	0.805	0.313	16.67	0.449	345.3	16.90	19.20	0.754	0.342	15.56	0.436	475.9	50.47		
		Rainy	23.98	0.853	0.285	17.20	0.512	231.6	20.17	18.62	0.786	0.327	14.95	0.498	612.2	62.22		
	Crowd	Low	26.03	0.842	0.280	17.02	0.465	225.6	24.65	22.77	0.803	0.309	15.73	0.459	380.3	71.86		
		High	20.92	0.784	0.328	14.98	0.397	794.6	27.28	18.20	0.743	0.357	13.95	0.384	893.1	59.59		
<i>Full</i>			22.72	0.812	0.307	15.82	0.425	433.2	22.62	18.91	0.761	0.343	14.32	0.409	682.2	58.52		
DeformGS [29] (2024)	Time	Noon	26.90	0.860	0.141	18.29	0.563	501.2	3.61	24.08	0.768	0.166	16.76	0.418	536.3	15.95		
		Dusk	26.35	0.875	0.128	16.24	0.427	445.1	5.54	24.80	0.823	0.140	15.56	0.346	931.1	19.41		
	Weather	Normal	27.83	0.884	0.121	19.68	0.625	294.6	3.55	25.09	0.803	0.145	18.43	0.501	419.9	15.33		
		Rainy	29.22	0.899	0.131	20.36	0.640	181.2	3.81	26.22	0.835	0.150	18.56	0.511	469.7	16.70		
	Crowd	Low	30.51	<b>0.908</b>	<b>0.099</b>	20.13	0.644	194.2	3.04	27.09	<b>0.831</b>	<b>0.120</b>	18.50	0.497	369.3	14.88		
		High	25.28	0.841	0.174	17.09	0.504	608.5	5.45	23.38	0.771	0.182	16.22	0.397	724.6	19.53		
<i>Full</i>			27.61	0.877	0.135	18.74	0.572	360.9	4.3	25.04	0.804	0.152	17.46	0.450	564.2	16.84		
StreetGS [26] (2024)	Time	Noon	27.96	0.870	<b>0.124</b>	20.81	0.729	172.9	1.97	25.21	0.781	0.146	18.40	0.518	210.1	12.29		
		Dusk	28.38	<b>0.889</b>	0.106	20.84	0.715	102.6	2.41	26.48	0.832	<b>0.121</b>	19.29	0.589	234.8	13.80		
	Weather	Normal	28.90	<b>0.890</b>	<b>0.108</b>	23.93	0.788	99.5	1.54	26.07	0.809	0.124	21.01	<b>0.592</b>	203.4	7.23		
		Rainy	29.68	0.900	0.124	23.23	0.765	60.6	2.00	26.91	0.839	<b>0.145</b>	20.56	0.593	207.4	12.52		
	Crowd	Low	30.89	0.903	0.102	23.14	0.771	46.5	2.11	27.71	0.828	0.121	20.28	0.561	123.7	12.21		
		High	27.61	0.868	0.131	21.58	0.737	137.6	2.13	25.09	0.784	0.156	19.29	0.550	253.2	13.29		
<i>Full</i>			28.88	0.886	0.116	22.54	0.758	103.0	2.01	26.20	0.812	0.135	20.01	0.572	214.8	11.47		
OMNIRE [3] (2025)	Time	Noon	28.16	<b>0.871</b>	<b>0.122</b>	20.97	<b>0.736</b>	<b>158.7</b>	<b>1.85</b>	25.33	<b>0.783</b>	<b>0.141</b>	18.43	0.517	<b>205.5</b>	<b>11.75</b>		
		Dusk	28.70	<b>0.889</b>	<b>0.105</b>	21.13	<b>0.727</b>	<b>46.7</b>	<b>2.24</b>	26.74	<b>0.833</b>	<b>0.121</b>	19.53	<b>0.599</b>	<b>71.4</b>	<b>13.22</b>		
	Weather	Normal	29.14	0.888	<b>0.108</b>	24.12	0.791	56.6	1.46	26.20	0.810	0.122	21.02	0.590	112.7	7.05		
		Rainy	30.06	<b>0.902</b>	<b>0.122</b>	24.04	0.779	35.1	1.79	27.20	0.838	0.146	21.20	0.604	<b>138.2</b>	<b>12.25</b>		
	Crowd	Low	<b>31.27</b>	0.904	0.101	23.95	0.792	<b>25.8</b>	2.02	<b>27.95</b>	0.828	<b>0.120</b>	<b>20.94</b>	0.585	<b>78.5</b>	<b>11.76</b>		
		High	<b>28.01</b>	<b>0.869</b>	<b>0.129</b>	21.83	0.741	89.3	2.03	25.34	0.788	0.146	19.42	0.551	170.5	12.58		
<i>Full</i>			<b>29.20</b>	<b>0.887</b>	<b>0.114</b>	22.90	<b>0.767</b>	<b>63.7</b>	<b>1.87</b>	<b>26.41</b>	0.813	<b>0.132</b>	<b>20.25</b>	<b>0.579</b>	<b>125.2</b>	<b>10.93</b>		
CRUISE [22] (2025)	Time	Noon	23.40	0.799	0.209	17.15	0.490	378.1	5.44	22.60	0.765	0.220	16.71	0.445	440.6	23.65		
		Dusk	24.01	0.821	0.193	18.91	0.591	147.9	5.45	23.51	0.804	0.196	16.67	0.444	452.5	24.50		
	Weather	Normal	24.19	0.822	0.184	19.39	0.601	277.4	5.33	23.00	0.793	0.199	18.39	0.514	336.7	25.08		
		Rainy	25.48	0.856	0.176	18.77	0.569	134.4	5.84	24.62	0.836	0.187	18.27	0.518	313.5	24.81		
	Crowd	Low	23.18	0.802	0.204	17.84	0.513	134.8	4.95	25.75	0.831	0.168	18.61	0.542	265.7	23.83		
		High	26.98	0.861	0.149	18.96	0.584	360.7	6.38	22.57	0.779	0.215	17.24	0.466	440.7	26.48		
<i>Full</i>			24.47	0.826	0.187	18.57	0.561	433.2	22.62	23.63	0.801	0.199	17.68	0.488	397.6	24.49		
PVG [2] (2026)	Time	Noon	<b>28.42</b>	0.858	0.174	<b>22.36</b>	0.734	185.6	2.21	<b>25.87</b>	<b>0.789</b>	0.193	<b>19.70</b>	<b>0.549</b>	323.5	12.38		
		Dusk	27.82	0.883	0.148	20.47	0.665	134.9	3.62	25.64	0.830	0.161	18.20	0.491	306.4	17.83		
	Weather	Normal	29.01	0.880	0.150	23.74	0.772	137.3	2.23	<b>26.28</b>	<b>0.817</b>	0.159	20.90	0.591	226.5	12.36		
		Rainy	<b>30.46</b>	0.900	0.149	<b>24.61</b>	<b>0.789</b>	51.5	2.39	<b>27.37</b>	<b>0.848</b>	0.164	<b>21.38</b>	<b>0.609</b>	194.6	13.75		
	Crowd	Low	<b>31.43</b>	0.903	0.120	<b>24.85</b>	<b>0.808</b>	46.1	<b>1.76</b>	27.53	<b>0.835</b>	0.137	<b>21.12</b>	<b>0.602</b>	121.4	14.57		
		High	27.06	0.852	0.189	21.27	0.675	248.3	3.86	24.72	0.787	0.203	19.15	0.520	410.0	16.14		
<i>Full</i>			28.97	0.879	0.157	<b>22.91</b>	0.742	131.9	2.77	26.16	<b>0.817</b>	0.171	20.09	0.562	262.3	14.24		
<b>Ours</b> <b>(DUST)</b>	Time	Noon	<b>28.75</b>	<b>0.872</b>	<b>0.122</b>	<b>24.11</b>	<b>0.839</b>	<b>78.1</b>	<b>1.65</b>	<b>25.94</b>	<b>0.789</b>	<b>0.137</b>	<b>20.04</b>	<b>0.584</b>	<b>167.5</b>	<b>9.14</b>		
		Dusk	<b>29.05</b>	<b>0.892</b>	<b>0.102</b>	<b>24.57</b>	<b>0.844</b>	<b>27.8</b>	<b>2.04</b>	<b>27.03</b>	<b>0.834</b>	<b>0.119</b>	<b>21.50</b>	<b>0.667</b>	<b>69.5</b>	<b>11.90</b>		
	Weather	Normal	<b>29.42</b>	<b>0.891</b>	<b>0.105</b>	<b>26.85</b>	<b>0.871</b>	<b>45.1</b>	<b>1.31</b>	<b>26.72</b>	<b>0.817</b>	<b>0.120</b>	<b>22.67</b>	<b>0.641</b>	<b>111.0</b>	<b>6.52</b>		
		Rainy	<b>30.36</b>	<b>0.904</b>	<b>0.119</b>	<b>27.86</b>	<b>0.880</b>	<b>21.8</b>	<b>1.62</b>	<b>27.49</b>	<b>0.842</b>	<b>0.141</b>	<b>22.44</b>	<b>0.640</b>	<b>84.6</b>	<b>11.82</b>		
	Crowd	Low	<b>31.43</b>	<b>0.906</b>	<b>0.098</b>	<b>27.61</b>	<b>0.878</b>	<b>18.1</b>	<b>1.74</b>	<b>28.18</b>	<b>0.831</b>	<b>0.118</b>	<b>22.40</b>	<b>0.627</b>	<b>46.0</b>	<b>11.44</b>		
		High	<b>28.56</b>	<b>0.872</b>	<b>0.125</b>	<b>24.49</b>	<b>0.829</b>	<b>47.4</b>	<b>1.90</b>	<b>25.90</b>	<b>0.794</b>	<b>0.145</b>	<b>21.01</b>	<b>0.613</b>	<b>105.3</b>	<b>10.80</b>		
<i>Full</i>			<b>29.55</b>	<b>0.889</b>	<b>0.112</b>	<b>26.11</b>	<b>0.860</b>	<b>39.7</b>	<b>1.70</b>	<b>26.82</b>	<b>0.818</b>	<b>0.130</b>	<b>21.80</b>	<b>0.631</b>	<b>97.2</b>	<b>9.94</b>		

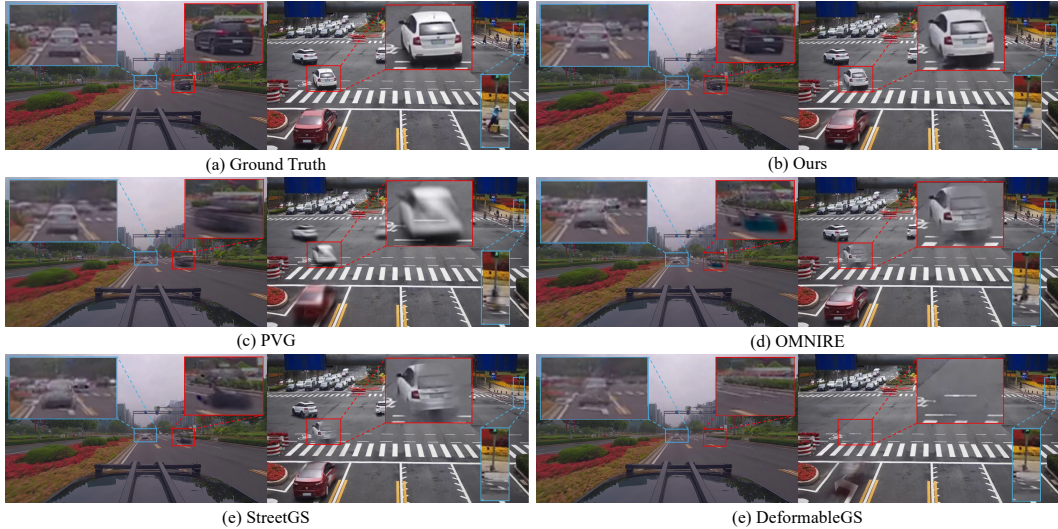


Figure 3: **Qualitative comparison on dynamic agents under asynchronous observations.** Compared to baselines, our method DUST achieves less ghosting and more high-quality reconstruction of various agents, including vehicles and pedestrians. The insets highlight the details.

37.7%, dropping it from 63.7 to 39.7. This temporal stability comes from both the DUST-GSG representation and our pose regularization, which jointly prevent trajectory jitter. Visual comparisons in Fig. 3 align with these numbers. While baselines suffer from severe ghosting and blurring on moving vehicles and pedestrians, DUST renders sharp and artifact-free dynamic agents.

### 4.3 Complex Driving Conditions

Tab. 1 shows our method is robust in complex environments. The gap is clearest in crowded scenes, where dense traffic creates more asynchronous conflicts. Baselines struggle here, but DUST achieves an FVD of 47.4, reducing OMNIRE’s score of 89.3 by nearly 47%. We also maintain a strong lead in dynamic areas during rainy weather and at dusk.

While DUST ranks second in a few full-image metrics, the difference is marginal. For example, our full-image PSNR in rainy conditions is only 0.1 dB lower than PVG. This slight drop is expected because full-image scores are dominated by static backgrounds, which existing methods already model well.

### 4.4 Asynchronous Observations

To evaluate robustness against asynchronous data, we introduce time delays between the two observation sources. Specifically, we pair the vehicle frames with infrastructure frames shifted by one to three time steps. This setup creates physical time gaps ranging from zero to 300 milliseconds. Fig. 4 compares DUST and StreetGS using PSNR and SSIM for both full images and dynamic areas. As the time gap increases, StreetGS performance drops rapidly. In contrast, DUST shows a much slower decay. This demonstrates that DUST has stronger robustness to temporal asynchrony. The figure also plots our cumulative advantage. This metric grows steadily with larger time delays. The widening gap confirms that our

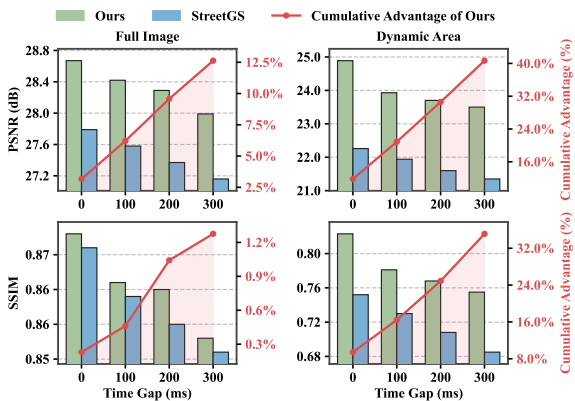


Figure 4: Performance comparison between Ours and StreetGS under increasing temporal asynchrony of 0-300 (Time Gap) ms. The cumulative growth rate of our method over StreetGS on the specified metrics is illustrated by the red curve.

decoupled design effectively handles severe asynchrony. It successfully prevents the motion artifacts common in single timeline methods.

#### 4.5 Ablation Studies

We conduct comprehensive ablation studies to evaluate the contribution of each module, with results shown in Tab. 2 and Fig. 5. The findings demonstrate the critical role of our proposed DUST-GSG representation. Removing either the dual timelines or the separated poses causes severe performance drops, especially in dynamic areas where the vehicle PSNR falls from 25.12 to 23.35 and 22.34, respectively. This confirms that decoupling spatio and temporal states is essential for handling asynchronous cooperative data. Furthermore, the static anchor-based pose correction provides crucial initialization. Without it, the dynamic PSNR decreases by 1.14 dB. This proves that refining the raw dataset labels is a necessary step before initializing the Gaussian trajectories.

Table 2: Ablations on the High Crowd scenes subset. Dual Timelines and Separated are the part of DUST-GSG

Variant	Full Image			Dynamic Area	
	PSNR↑	SSIM↑	LPIPS↓	PSNR↑	SSIM↑
Full Model	<b>28.75</b>	<b>0.874</b>	<b>0.125</b>	<b>25.12</b>	<b>0.837</b>
w/o Pose correction	27.91	0.873	0.128	23.98	0.821
w/o Dual Timelines	28.40	0.872	0.128	23.35	0.783
w/o Separated Poses	28.19	0.870	0.131	22.34	0.742
w/o $\mathcal{L}_{\text{drift}}$	28.72	0.873	0.126	24.99	0.832
w/o $\mathcal{L}_{\text{smooth}}$	28.62	0.869	0.134	24.96	0.833

Without the pose regularization ( $\mathcal{L}_{\text{smooth}}$ ), the LPIPS falls from 0.125 to 0.134. This demonstrates that applying the smooth regularization to the pose is crucial for refined reconstruction. Finally, while removing the pose regularization ( $\mathcal{L}_{\text{drift}}$ ) causes only a slight drop in PSNR, this term is vital for dynamic stability. As shown in Fig. 5e, without this constraint, unconstrained joint optimization leads to trajectory drift and jittering during early training. The regularization ensures the Gaussians learn correct appearances rather than compensating for incorrect positions. Together, these modules allow DUST to effectively reconstruct dynamic objects and establish a strong decoupled paradigm for VICAD reconstruction.



Figure 5: **Qualitative ablation study** results across infrastructure camera from the scene reconstruction task. (a) Our complete model. (b) Without pose initialization before decoupling. (c) Without dual timelines. (d) Without separated poses. (e) Without  $\mathcal{L}_{\text{drift}}$ . (f) Without  $\mathcal{L}_{\text{smooth}}$ .

## 5 Conclusion

We present **DUST**. It is a cooperative reconstruction framework designed for asynchronous autonomous driving scenarios. We mathematically prove that using a single timeline inherently causes reconstruction errors. To resolve this, we introduce a decoupled scene graph. We combine this core design with anchor based pose correction and spatio pose regularization. Extensive experiments on the V2X Seq dataset show that our method achieves superior performance across various asynchronous conditions. Our current framework has a limitation. Our decoupled design successfully resolves the trajectory mismatch for dynamic agents. However, it does not explicitly handle the shape changes of deformable objects like pedestrians under asynchronous observations. Time delays can still cause appearance blur during rapid limb movements. Future research will explore feature based fine grained temporal deformation modeling.

## References

- [1] Ang Cao and Justin Johnson. Hexplane: A fast representation for dynamic scenes. In *Proceedings of the IEEE/CVF Conference on Computer Vision and Pattern Recognition*, pages 130–141, 2023.
- [2] Yurui Chen, Chun Gu, Junzhe Jiang, Xiatian Zhu, and Li Zhang. Periodic vibration gaussian: Dynamic urban scene reconstruction and real-time rendering. *International Journal of Computer Vision*, 134(3):83, 2026.
- [3] Ziyu Chen, Jiawei Yang, Jiahui Huang, Riccardo De Lutio, Janick Martinez Esturo, Boris Ivanovic, Or Litany, Zan Gojcic, Sanja Fidler, Marco Pavone, et al. Omnire: Omni urban scene reconstruction. In *International Conference on Learning Representations*, volume 2025, pages 85508–85527, 2025.
- [4] Sara Fridovich-Keil, Giacomo Meanti, Frederik Rahbæk Warburg, Benjamin Recht, and Angjoo Kanazawa. K-planes: Explicit radiance fields in space, time, and appearance. In *Proceedings of the IEEE/CVF conference on computer vision and pattern recognition*, pages 12479–12488, 2023.
- [5] Chen Gao, Ayush Saraf, Johannes Kopf, and Jia-Bin Huang. Dynamic view synthesis from dynamic monocular video. In *Proceedings of the IEEE/CVF International Conference on Computer Vision*, pages 5712–5721, 2021.
- [6] Yue Hu, Shaoheng Fang, Zixing Lei, Yiqi Zhong, and Siheng Chen. Where2comm: Communication-efficient collaborative perception via spatial confidence maps. *Advances in neural information processing systems*, 35:4874–4886, 2022.
- [7] Bernhard Kerbl, Georgios Kopanas, Thomas Leimkühler, George Drettakis, et al. 3d gaussian splatting for real-time radiance field rendering. *ACM Trans. Graph.*, 42(4):139–1, 2023.
- [8] H. W. Kuhn. The hungarian method for the assignment problem. *Naval Research Logistics Quarterly*, page 83–97, 1955.
- [9] Yiming Li, Shunli Ren, Pengxiang Wu, Siheng Chen, Chen Feng, and Wenjun Zhang. Learning distilled collaboration graph for multi-agent perception. *Advances in Neural Information Processing Systems*, 34:29541–29552, 2021.
- [10] Zhengqi Li, Simon Niklaus, Noah Snavely, and Oliver Wang. Neural scene flow fields for space-time view synthesis of dynamic scenes. In *Proceedings of the IEEE/CVF conference on computer vision and pattern recognition*, pages 6498–6508, 2021.
- [11] Yang Lu, Jie Wang, Xiaoyun Dong, Ziyao Huang, Bingyi Liu, Jen-Ming Wu, and Jianping Wang. Vi-planning: Infrastructure-assisted real-time planning optimization for autonomous driving. In *Proceedings of the 31st Annual International Conference on Mobile Computing and Networking*, pages 923–937, 2025.
- [12] Yifan Lu, Quanhao Li, Baoan Liu, Mehrdad Dianati, Chen Feng, Siheng Chen, and Yanfeng Wang. Robust collaborative 3d object detection in presence of pose errors. *arXiv preprint arXiv:2211.07214*, 2022.
- [13] Albert Pumarola, Enric Corona, Gerard Pons-Moll, and Francesc Moreno-Noguer. D-nerf: Neural radiance fields for dynamic scenes. In *Proceedings of the IEEE/CVF conference on computer vision and pattern recognition*, pages 10318–10327, 2021.
- [14] Dewi Retno Sari Saputro and Purnami Widyaningsih. Limited memory broyden-fletcher-goldfarb-shanno (l-bfgs) method for the parameter estimation on geographically weighted ordinal logistic regression model (gwolr). In *AIP conference proceedings*, volume 1868, page 040009. AIP Publishing LLC, 2017.
- [15] Shuyao Shi, Jiahe Cui, Zehao Jiang, Zhenyu Yan, Guoliang Xing, Jianwei Niu, and Zhenchao Ouyang. Vips: Real-time perception fusion for infrastructure-assisted autonomous driving. In *Proceedings of the 28th annual international conference on mobile computing and networking*, pages 133–146, 2022.

- [16] Ken Shoemake. Animating rotation with quaternion curves. In *Proceedings of the 12th annual conference on Computer graphics and interactive techniques*, pages 245–254, 1985.
- [17] Zachary Teed and Jia Deng. Raft: Recurrent all-pairs field transforms for optical flow. In *European conference on computer vision*, pages 402–419. Springer, 2020.
- [18] Thomas Unterthiner, Sjoerd Van Steenkiste, Karol Kurach, Raphael Marinier, Marcin Michalski, and Sylvain Gelly. Towards accurate generative models of video: A new metric & challenges. *arXiv preprint arXiv:1812.01717*, 2018.
- [19] Zhou Wang, A.C. Bovik, H.R. Sheikh, and E.P. Simoncelli. Image quality assessment: from error visibility to structural similarity. *IEEE Transactions on Image Processing*, 13(4):600–612, 2004.
- [20] GuanJun Wu, Taoran Yi, Jiemin Fang, Lingxi Xie, Xiaopeng Zhang, Wei Wei, Wenyu Liu, Qi Tian, and Xinggang Wang. 4d gaussian splatting for real-time dynamic scene rendering. In *Proceedings of the IEEE/CVF conference on computer vision and pattern recognition*, pages 20310–20320, 2024.
- [21] Hao Xiang, Zhaoliang Zheng, Xin Xia, Runsheng Xu, Letian Gao, Zewei Zhou, Xu Han, Xinkai Ji, Mingxi Li, Zonglin Meng, et al. V2x-real: a largs-scale dataset for vehicle-to-everything cooperative perception. In *European Conference on Computer Vision*, pages 455–470. Springer, 2024.
- [22] Haoran Xu, Saining Zhang, Peishuo Li, Baijun Ye, Xiaoxue Chen, Huan-ang Gao, Jv Zheng, Xiaowei Song, Ziqiao Peng, Run Miao, et al. Cruise: Cooperative reconstruction and editing in v2x scenarios using gaussian splatting. In *2025 IEEE/RSJ International Conference on Intelligent Robots and Systems (IROS)*, pages 12518–12525. IEEE, 2025.
- [23] Runsheng Xu, Hao Xiang, Zhengzhong Tu, Xin Xia, Ming-Hsuan Yang, and Jiaqi Ma. V2x-vit: Vehicle-to-everything cooperative perception with vision transformer. In *European conference on computer vision*, pages 107–124. Springer, 2022.
- [24] Runsheng Xu, Hao Xiang, Xin Xia, Xu Han, Jinlong Li, and Jiaqi Ma. Opv2v: An open benchmark dataset and fusion pipeline for perception with vehicle-to-vehicle communication. In *2022 International Conference on Robotics and Automation (ICRA)*, pages 2583–2589, 2022.
- [25] Yunjiang Xu, Lingzhi Li, Jin Wang, Yupeng Ouyang, and Benyuan Yang. Instinct: Instance-level interaction architecture for query-based collaborative perception. In *Proceedings of the IEEE/CVF International Conference on Computer Vision*, pages 25464–25473, 2025.
- [26] Yunzhi Yan, Haotong Lin, Chenxu Zhou, Weijie Wang, Haiyang Sun, Kun Zhan, Xianpeng Lang, Xiaowei Zhou, and Sida Peng. Street gaussians: Modeling dynamic urban scenes with gaussian splatting. In *European Conference on Computer Vision*, pages 156–173. Springer, 2024.
- [27] Jiawei Yang, Boris Ivanovic, Or Litany, Xinshuo Weng, Seung Wook Kim, Boyi Li, Tong Che, Danfei Xu, Sanja Fidler, Marco Pavone, et al. Emernerf: Emergent spatial-temporal scene decomposition via self-supervision. *arXiv preprint arXiv:2311.02077*, 2023.
- [28] Lei Yang, Kaicheng Yu, Tao Tang, Jun Li, Kun Yuan, Li Wang, Xinyu Zhang, and Peng Chen. Bevheight: A robust framework for vision-based roadside 3d object detection. In *IEEE/CVF Conf. on Computer Vision and Pattern Recognition (CVPR)*, March 2023.
- [29] Ziyi Yang, Xinyu Gao, Wen Zhou, Shaohui Jiao, Yuqing Zhang, and Xiaogang Jin. Deformable 3d gaussians for high-fidelity monocular dynamic scene reconstruction. In *Proceedings of the IEEE/CVF conference on computer vision and pattern recognition*, pages 20331–20341, 2024.
- [30] Haibao Yu, Yizhen Luo, Mao Shu, Yiyi Huo, Zebang Yang, Yifeng Shi, Zhenglong Guo, Hanyu Li, Xing Hu, Jirui Yuan, and Zaiqing Nie. Dair-v2x: A large-scale dataset for vehicle-infrastructure cooperative 3d object detection. In *Proceedings of the IEEE/CVF Conference on Computer Vision and Pattern Recognition*, pages 21361–21370, 2022.

- [31] Haibao Yu, Wenxian Yang, Hongzhi Ruan, Zhenwei Yang, Yingjuan Tang, Xu Gao, Xin Hao, Yifeng Shi, Yifeng Pan, Ning Sun, Juan Song, Jirui Yuan, Ping Luo, and Zaiqing Nie. V2x-seq: A large-scale sequential dataset for vehicle-infrastructure cooperative perception and forecasting. In *Proceedings of the IEEE/CVF Conference on Computer Vision and Pattern Recognition*, 2023.
- [32] Haibao Yu, Wenxian Yang, Jiaru Zhong, Zhenwei Yang, Siqu Fan, Ping Luo, and Zaiqing Nie. End-to-end autonomous driving through v2x cooperation. In *The 39th Annual AAAI Conference on Artificial Intelligence*, 2025.
- [33] Richard Zhang, Phillip Isola, Alexei A Efros, Eli Shechtman, and Oliver Wang. The unreasonable effectiveness of deep features as a perceptual metric. In *CVPR*, 2018.
- [34] Xiaoyu Zhou, Zhiwei Lin, Xiaojun Shan, Yongtao Wang, Deqing Sun, and Ming-Hsuan Yang. Drivinggaussian: Composite gaussian splatting for surrounding dynamic autonomous driving scenes. In *Proceedings of the IEEE/CVF Conference on Computer Vision and Pattern Recognition*, pages 21634–21643, 2024.
- [35] Yi Zhou, Connelly Barnes, Jingwan Lu, Jimei Yang, and Hao Li. On the continuity of rotation representations in neural networks. In *Proceedings of the IEEE/CVF conference on computer vision and pattern recognition*, pages 5745–5753, 2019.

# Appendices

<b>A Notation</b>	<b>13</b>
<b>B Proof</b>	<b>15</b>
B.1 Formal Rendering Model and Assumptions . . . . .	15
B.2 Jacobian Structure and Rendering Fisher Information . . . . .	15
B.3 Proof of Part (i): Irreducible Residual under Single-Timeline . . . . .	16
B.4 Proof of Part (ii): Gradient Incompatibility . . . . .	17
B.5 Proof of Part (iii): NTK Block-Diagonalization . . . . .	18
<b>C Implementation Details</b>	<b>20</b>
C.1 Initialization . . . . .	20
C.2 Training . . . . .	20
C.3 Optimization . . . . .	20
<b>D Evaluation</b>	<b>21</b>
D.1 Datasets . . . . .	21
D.2 Metrics . . . . .	21
D.3 Baselines . . . . .	23

## A Notation

Table 3: Notation used in the main paper and appendix.

<i>Notation</i>	<i>Definition</i>
<b>INDICES &amp; TEMPORAL QUANTITIES</b>	
$c \in \{v, f\}$	Source index: $v$ for vehicle, $f$ for infrastructure
$n = 1, \dots, N$	Index over canonical Gaussians of a single dynamic agent
$t_i$	$i$ -th cooperative anchor timestamp
$\tau_c$	Actual sensor capture time of source $c$
$\Delta\tau$	Temporal offset between sources: $\Delta\tau = \tau_v - \tau_f$
$v \in \mathbb{R}^3$	Agent velocity vector under locally rigid motion
<b>CANONICAL-SPACE PARAMETERS (ORANGE)</b>	
$\bar{\mu}_n \in \mathbb{R}^3$	Canonical mean of Gaussian $n$ in the agent’s body frame
$\bar{\mu}_n^* \in \mathbb{R}^3$	Ground-truth canonical mean of Gaussian $n$ ; shared across all sources
$\bar{\Sigma}_n \in \mathbb{S}_{++}^3, \bar{\alpha}_n, \bar{c}_n$	Canonical covariance, opacity, and color coefficient of Gaussian $n$
$w_n^c(u)$	Alpha-compositing blending weight of Gaussian $n$ at pixel $u$ from source $c$
$\phi_n^c(u) \in \mathbb{R}^3$	Pixel-space influence vector of Gaussian $n$ at pixel $u$ from source $c$ (Eq. 15)
$\mathbf{A}_n^c \in \mathbb{S}_+^3$	Rendering Fisher information matrix: $\mathbf{A}_n^c = \sum_{u \in \mathcal{U}^c} \phi_n^c(u) \phi_n^c(u)^\top$ (Def. 5)
$\lambda_{\min, n}, \lambda_n$	Minimum Fisher eigenvalue: $\min(\lambda_{\min}(\mathbf{A}_n^v), \lambda_{\min}(\mathbf{A}_n^f))$
<b>POSE &amp; WORLD-SPACE QUANTITIES (BLUE)</b>	
$R^c \in SO(3), T^c \in \mathbb{R}^3$	Rotation and translation of source $c$ at capture time $\tau_c$
$R_i, T_i$	Shared rotation and translation in the single-timeline formulation at anchor $t_i$

Table 3 (continued)

Notation	Definition
$\mu_n^c \in \mathbb{R}^3$	World-space mean of Gaussian $n$ from source $c$ : $\mu_n^c = R^c \bar{\mu}_n + T^c$
$\mu_n^{*,c} \in \mathbb{R}^3$	Ground-truth world position of Gaussian $n$ at capture time $\tau_c$
$\mu_n^\dagger \in \mathbb{R}^3$	Fisher-weighted optimal world position under single-timeline (Eq. 24)
$\delta_n^c \in \mathbb{R}^3$	World-space positional error: $\delta_n^c = \mu_n^c - \mu_n^{*,c}$
$\delta_n^{c\dagger} \in \mathbb{R}^3$	Residual positional error at the single-timeline optimum $\mu_n^\dagger$
$J_{\pi,n}^c \in \mathbb{R}^{2 \times 3}$	Jacobian of camera projection at $\mu_n^c$ : $J_{\pi,n}^c = \partial \hat{u}_n^c / \partial \mu_n^c$
$\hat{u}_n^c \in \mathbb{R}^2, \hat{\Sigma}_n^c \in \mathbb{S}_{++}^2$	Projected 2D mean and covariance of Gaussian $n$ in source $c$ 's image plane (EWA splatting)
$\xi^v, \xi^f \in \mathbb{R}^6$	Source-specific pose parameters in $\mathfrak{se}(3)$ under DUST-GSG; collapsed to a single shared $\xi$ under single-timeline
<b>NTK QUANTITIES</b>	
$\theta = (\bar{\mu}, \xi)$	Full optimizable parameter vector
$\Theta \in \mathbb{R}^{M \times M}$	Empirical Neural Tangent Kernel matrix
$\Theta^{\bar{\mu}}, \Theta^\xi$	Canonical-parameter and pose-parameter additive components of $\Theta$
$\Theta_{vv}^{\xi^v}, \Theta_{ff}^{\xi^f}$	Vehicle and infrastructure diagonal blocks of the DUST-GSG pose kernel
$\mathbf{r}^c(t)$	Pixel residual vector of source $c$ at training step $t$ : $\mathbf{r}^c(t) = \hat{\mathbf{I}}^c(t) - \mathbf{I}^{c*}$
<b>RENDERING &amp; PHOTOMETRIC LOSS</b>	
$\hat{I}^c(u)$	Rendered color at pixel $u$ from source $c$
$I^{c*}(u)$	Ground-truth image captured at time $\tau_c$
$\mathcal{U}^c$	Set of pixels observing the agent from source $c$
$\mathcal{L}^c$	Per-source photometric loss
$\mathcal{L}_n^c$	Per-Gaussian per-source loss (quadratic form)
$\mathcal{L}_{\text{single}}^*$	Optimal reconstruction loss under single-timeline
$\mathcal{L}_{\text{DST}}^*$	Optimal reconstruction loss under DUST
<b>LOSS FUNCTIONS &amp; REGULARIZATION</b>	
$\mathcal{L}_{\text{image}}$	Image loss: $(1 - \lambda_r)\mathcal{L}_1 + \lambda_r\mathcal{L}_{\text{SSIM}}$
$\mathcal{L}_1$	L1 reconstruction loss
$\mathcal{L}_{\text{SSIM}}$	SSIM reconstruction loss
$\lambda_r = 0.2$	Weight of the SSIM loss
$\mathcal{L}_{\text{depth}}$	Depth map loss: $\frac{1}{hw} \sum \ \mathcal{D}^s - \hat{\mathcal{D}}\ _1$
$\mathcal{D}^s$	Inverse of the sparse LiDAR depth map
$\hat{\mathcal{D}}$	Inverse of the predicted depth map
$\mathcal{L}_{\text{opacity}}$	Mask/opacity loss (sky + occupancy)
$O_g$	Rendered opacity map
$M_{\text{sky}}$	Sky mask
$\mathcal{L}_{\text{reg}}$	Pose smoothness regularization
$\theta(t)$	Human body poses at time $t$
$\delta$	Randomly chosen integer from $\{1, 2, 3, 4, 5\}$ for pose regularization
$\lambda_{\text{depth}} = 0.01$	Weight of depth loss
$\lambda_{\text{opacity}} = 0.05$	Weight of opacity loss
$\lambda_{\text{reg}} = 0.01$	Weight of pose smoothness loss
<b>EVALUATION METRICS</b>	
$\hat{\mathbf{I}}$	Rendered image
$\mathbf{I}$	Ground-truth image
$N$	Number of valid pixels (in PSNR computation)
$\mu_x, \mu_y$	Local means of image patches $\mathbf{x}, \mathbf{y}$ (SSIM)
$\sigma_x, \sigma_y$	Local standard deviations (SSIM)
$\sigma_{xy}$	Local cross-covariance (SSIM)
$c_1, c_2$	Small constants for numerical stability (SSIM)
$\phi_\ell(\cdot)$	Feature map from layer $\ell$ of AlexNet (LPIPS)
$\mathbf{w}_\ell$	Learned channel-wise weights at layer $\ell$ (LPIPS)
$H_\ell, W_\ell$	Spatial dimensions of feature map at layer $\ell$ (LPIPS)
$\boldsymbol{\mu}_{\text{gen}}, \boldsymbol{\Sigma}_{\text{gen}}$	Mean and covariance of generated video clip features (FVD)
$\boldsymbol{\mu}_{\text{real}}, \boldsymbol{\Sigma}_{\text{real}}$	Mean and covariance of real video clip features (FVD)
$T$	Total number of video frames
$T_c = 16$	Length of each non-overlapping video clip (FVD)
$\mathbf{F}_t \in \mathbb{R}^{H \times W \times 2}$	Dense optical flow field between frames $t$ and $t + 1$
$(u, v)$	Horizontal and vertical components of optical flow

Table 3 (continued)

Notation	Definition
$(\hat{u}, \hat{v})$	Predicted flow components (rendered video)
$\mathcal{M}$	Union of dynamic masks from two consecutive frames (EPE)

## B Proof

We provide a rigorous proof that the DUST-GSG formulation eliminates the fundamental optimization conflict inherent in single-timeline representations under asynchronous vehicle–infrastructure observations. The proof proceeds in five stages: we first formalize the rendering model and state the working assumptions (§B.1); then derive the Jacobian structure and the rendering Fisher information matrix (§B.2); next prove the irreducible-residual lower bound (§B.3); then establish gradient incompatibility (§B.4); and finally show how DUST-GSG resolves both issues via NTK block-diagonalization (§B.5).

### B.1 Formal Rendering Model and Assumptions

Throughout the proof, **orange** denotes *canonical-space* quantities (those defined in the agent’s body frame, independent of capture time), and **blue** denotes *pose/world-space* quantities (those that depend on the source-specific rigid-body transform or the camera).

**Definition 2** (Canonical Gaussian Agent). *A dynamic agent is represented by  $N$  canonical 3D Gaussians with means  $\bar{\mu} = (\bar{\mu}_1, \dots, \bar{\mu}_N) \in \mathbb{R}^{3N}$ , covariances  $\bar{\Sigma} = (\bar{\Sigma}_1, \dots, \bar{\Sigma}_N)$  with each  $\bar{\Sigma}_n \in \mathbb{S}_{++}^3$ , opacities  $\bar{\alpha} = (\bar{\alpha}_1, \dots, \bar{\alpha}_N) \in (0, 1)^N$ , and view-dependent color coefficients  $\bar{c} = (\bar{c}_1, \dots, \bar{c}_N)$ .*

**Definition 3** (Source-Specific World Projection). *For source  $c \in \{v, f\}$  (vehicle, infrastructure) with rigid-body pose  $P^c = (R^c, T^c) \in SE(3)$  at capture time  $\tau_c$ , the world-space parameters of Gaussian  $n$  are*

$$\mu_n^c = R^c \bar{\mu}_n + T^c, \quad \Sigma_n^c = R^c \bar{\Sigma}_n (R^c)^\top. \quad (9)$$

**Definition 4** (Differentiable Splatting Renderer). *Given camera intrinsics  $K^c \in \mathbb{R}^{3 \times 3}$  and extrinsics  $W^c \in SE(3)$ , the rendered color at pixel  $u \in \mathbb{R}^2$  from source  $c$  is*

$$\hat{I}^c(u) = \sum_{n=1}^N \underbrace{\bar{\alpha}_n \prod_{m < n} (1 - \bar{\alpha}_m \mathcal{G}_m^c(u))}_{w_n^c(u)} \bar{c}_n \mathcal{G}_n^c(u), \quad (10)$$

where  $\mathcal{G}_n^c(u) = \exp(-\frac{1}{2}(u - \hat{u}_n^c)^\top (\hat{\Sigma}_n^c)^{-1} (u - \hat{u}_n^c))$  is the 2D Gaussian evaluated at pixel  $u$ , with projected mean  $\hat{u}_n^c = \pi(K^c W^c \mu_n^c)$  and projected covariance  $\hat{\Sigma}_n^c$  obtained via EWA splatting. The blending weight  $w_n^c(u)$  encapsulates the front-to-back alpha-compositing logic.

**Assumption 1** (Linearized Rendering Regime). *We approximate the rendering function by its first-order Taylor expansion around the current parameters  $\theta_0$ . This characterizes the early training phase where gradient conflicts are most damaging:*

$$\hat{I}^c(u; \theta) \approx \hat{I}^c(u; \theta_0) + \langle \nabla_{\theta} \hat{I}^c(u; \theta_0), \theta - \theta_0 \rangle. \quad (11)$$

**Assumption 2** (Locally Rigid Motion). *During the temporal offset  $\Delta\tau = \tau_v - \tau_f$  between the two sources, the agent undergoes approximately constant-velocity motion with velocity  $v \in \mathbb{R}^3$ :*

$$\mu_n^*(\tau_f) \approx \mu_n^*(\tau_v) + v \cdot \Delta\tau, \quad \forall n = 1, \dots, N, \quad (12)$$

where  $\mu_n^*(\tau_c)$  denotes the ground-truth world position of Gaussian  $n$  at time  $\tau_c$ .

### B.2 Jacobian Structure and Rendering Fisher Information

From the rendering equation (10), the gradient of  $\hat{I}^c(u)$  with respect to  $\bar{\mu}_n$  factors through three stages via the chain rule:

$$\nabla_{\bar{\mu}_n} \hat{I}^c(u) = \underbrace{(R^c)^\top}_{\text{world} \rightarrow \text{canonical}} \cdot \underbrace{(J_{\pi, n}^c)^\top}_{\text{image} \rightarrow \text{world}} \cdot \underbrace{\nabla_{\hat{u}_n^c} \hat{I}^c(u)}_{\text{color} \rightarrow \text{image}} \in \mathbb{R}^3, \quad (13)$$

where  $J_{\pi, n}^c = \frac{\partial \hat{u}_n^c}{\partial \mu_n^c} \in \mathbb{R}^{2 \times 3}$  is the Jacobian of the camera projection evaluated at  $\mu_n^c$ , and  $\nabla_{\hat{u}_n^c} \hat{I}^c(u) \in \mathbb{R}^2$  is the sensitivity of the rendered color to the projected Gaussian center.

Differentiating Eq. (10) with respect to  $\hat{u}_n^c$ :

$$\nabla_{\hat{u}_n^c} \hat{I}^c(u) \approx w_n^c(u) \bar{c}_n \mathcal{G}_n^c(u) (\hat{\Sigma}_n^c)^{-1} (u - \hat{u}_n^c) \in \mathbb{R}^2. \quad (14)$$

The sensitivity is proportional to the blending weight  $w_n^c(u)$ , the Gaussian kernel value  $\mathcal{G}_n^c(u)$ , and the Mahalanobis displacement  $(u - \hat{u}_n^c)$  scaled by the inverse projected covariance. Pixels far from the Gaussian center or occluded by other Gaussians contribute negligibly.

Substituting Eq. (14) into Eq. (13) and defining the *pixel-space influence vector*

$$\phi_n^c(u) := (J_{\pi,n}^c)^\top w_n^c(u) \bar{c}_n \mathcal{G}_n^c(u) (\hat{\Sigma}_n^c)^{-1} (u - \hat{u}_n^c) \in \mathbb{R}^3, \quad (15)$$

we obtain the compact form

$$\nabla_{\bar{\mu}_n} \hat{I}^c(u) = (R^c)^\top \phi_n^c(u). \quad (16)$$

By Eq. (16), the gradient in canonical space equals the world-space influence vector  $\phi_n^c(u)$  rotated back by  $(R^c)^\top$ . This factorization is the structural key of the entire proof: since  $R^v \neq R^f$  in general, the same canonical parameter  $\bar{\mu}_n$  is pulled in two *different rotated directions* by the two sources—the geometric root of the gradient conflict exposed in Part (ii).

Consider the per-source photometric loss  $\mathcal{L}^c = \frac{1}{2} \sum_{u \in \mathcal{U}^c} (\hat{I}^c(u) - I^{c*}(u))^2$ , where  $\mathcal{U}^c$  is the set of pixels observing the agent from source  $c$  and  $I^{c*}$  is the ground-truth image captured at time  $\tau_c$ . The gradient with respect to  $\bar{\mu}_n$  is

$$\nabla_{\bar{\mu}_n} \mathcal{L}^c = (R^c)^\top \sum_{u \in \mathcal{U}^c} (\hat{I}^c(u) - I^{c*}(u)) \phi_n^c(u). \quad (17)$$

Under Assumption 1, the photometric residual at pixel  $u$  is dominated by the world-space positional error  $\delta_n^c = \mu_n^c - \mu_n^{*,c}$  of Gaussian  $n$ . A first-order expansion of the rendering equation around the true position yields  $\hat{I}^c(u) - I^{c*}(u) \approx \phi_n^c(u)^\top \delta_n^c$  (contribution from Gaussian  $n$ ). Substituting into Eq. (17), the gradient becomes

$$\nabla_{\bar{\mu}_n} \mathcal{L}^c \approx (R^c)^\top \underbrace{\left( \sum_{u \in \mathcal{U}^c} \phi_n^c(u) \phi_n^c(u)^\top \right)}_{\mathbf{A}_n^c \in \mathbb{R}^{3 \times 3}} \delta_n^c. \quad (18)$$

**Definition 5** (Rendering Fisher Information Matrix). *The rendering Fisher information matrix of Gaussian  $n$  from source  $c$  is*

$$\mathbf{A}_n^c = \sum_{u \in \mathcal{U}^c} \phi_n^c(u) \phi_n^c(u)^\top \in \mathbb{S}_+^3. \quad (19)$$

Being a sum of rank-1 outer products,  $\mathbf{A}_n^c$  is positive semi-definite by construction. It becomes strictly positive definite ( $\mathbf{A}_n^c \succ 0$ ) whenever  $\{\phi_n^c(u)\}_{u \in \mathcal{U}^c}$  spans  $\mathbb{R}^3$ , which holds when the agent is observed from a non-degenerate viewpoint with sufficient pixel coverage. We assume  $\mathbf{A}_n^c \succ 0$  throughout. Combining Eq. (19) with the residual approximation, the per-source loss for Gaussian  $n$  takes the quadratic form

$$\mathcal{L}_n^c \approx \frac{1}{2} (\delta_n^c)^\top \mathbf{A}_n^c \delta_n^c, \quad (20)$$

and the total per-source loss is  $\mathcal{L}^c = \sum_{n=1}^N \mathcal{L}_n^c$ . This quadratic structure is the foundation for all subsequent analyses.

### B.3 Proof of Part (i): Irreducible Residual under Single-Timeline

In the single-timeline formulation, both sources share pose  $P(t_i) = (R_i, T_i)$  at the anchor timestamp  $t_i$ , so the world-space position of every Gaussian is the same for both sources:  $\mu_n^v = \mu_n^f = R_i \bar{\mu}_n + T_i$ . However, the ground-truth positions differ between the two capture times. Under Assumption 2:

$$\mu_n^{*,v} = \mu_n^*(t_i) + v(\tau_v - t_i), \quad \mu_n^{*,f} = \mu_n^*(t_i) + v(\tau_f - t_i). \quad (21)$$

Denoting the shared world position as  $\mu_n = R_i \bar{\mu}_n + T_i$ , the positional errors for the two sources are

$$\begin{aligned} \delta_n^v &= \mu_n - \mu_n^{*,v} = (\mu_n - \mu_n^*(t_i)) - v(\tau_v - t_i), \\ \delta_n^f &= \mu_n - \mu_n^{*,f} = (\mu_n - \mu_n^*(t_i)) - v(\tau_f - t_i). \end{aligned} \quad (22)$$

Crucially, the difference between the two errors is *independent of the parameters*:

$$\delta_n^v - \delta_n^f = -v \Delta\tau, \quad \Delta\tau = \tau_v - \tau_f. \quad (23)$$

This identity is the root cause of the optimization conflict: no matter how we adjust  $\bar{\mu}_n$ , the two positional errors always differ by the fixed vector  $-v \Delta\tau$ . The optimizer therefore faces an irreconcilable constraint—reducing  $\delta_n^v$  necessarily increases  $\delta_n^f$  by the same amount, and vice versa.

The total loss for Gaussian  $n$  under single-timeline is  $\mathcal{L}_n = \mathcal{L}_n^v + \mathcal{L}_n^f = \frac{1}{2}(\delta_n^v)^\top \mathbf{A}_n^v \delta_n^v + \frac{1}{2}(\delta_n^f)^\top \mathbf{A}_n^f \delta_n^f$ . We minimize over  $\mu_n \in \mathbb{R}^3$  by setting  $\nabla_{\mu_n} \mathcal{L}_n = \mathbf{A}_n^v \delta_n^v + \mathbf{A}_n^f \delta_n^f = \mathbf{0}$ , and solving for the optimal position:

$$\begin{aligned} \mathbf{A}_n^v (\mu_n - \mu_n^{*,v}) + \mathbf{A}_n^f (\mu_n - \mu_n^{*,f}) &= \mathbf{0} \\ (\mathbf{A}_n^v + \mathbf{A}_n^f) \mu_n &= \mathbf{A}_n^v \mu_n^{*,v} + \mathbf{A}_n^f \mu_n^{*,f} \\ \mu_n^\dagger &= (\mathbf{A}_n^v + \mathbf{A}_n^f)^{-1} (\mathbf{A}_n^v \mu_n^{*,v} + \mathbf{A}_n^f \mu_n^{*,f}). \end{aligned} \quad (24)$$

This is the Fisher-weighted average of the two target positions—a compromise that is optimal for neither source individually. Substituting  $\mu_n^\dagger$  back, the residual errors at the optimum are

$$\begin{aligned} \delta_n^{v\dagger} &= \mu_n^\dagger - \mu_n^{*,v} \\ &= (\mathbf{A}_n^v + \mathbf{A}_n^f)^{-1} (\mathbf{A}_n^v \mu_n^{*,v} + \mathbf{A}_n^f \mu_n^{*,f}) - \mu_n^{*,v} \\ &= (\mathbf{A}_n^v + \mathbf{A}_n^f)^{-1} \mathbf{A}_n^f (\mu_n^{*,f} - \mu_n^{*,v}) \\ &= (\mathbf{A}_n^v + \mathbf{A}_n^f)^{-1} \mathbf{A}_n^f (-v\Delta\tau), \end{aligned} \quad (25)$$

where the last step uses  $\mu_n^{*,f} - \mu_n^{*,v} = -v\Delta\tau$  from Eqs. (21)–(23). Similarly,  $\delta_n^{f\dagger} = (\mathbf{A}_n^v + \mathbf{A}_n^f)^{-1} \mathbf{A}_n^v (v\Delta\tau)$ . Both residual errors are non-zero whenever  $v\Delta\tau \neq \mathbf{0}$ , confirming that the Fisher-weighted compromise leaves both sources with unresolved positional error.

We now derive the lower bound in two steps.

*Step A (eigenvalue inequality).* For any  $M \succ 0$  and any vector  $x$ ,  $x^\top M x \geq \lambda_{\min}(M) \|x\|^2$ . Applying this at the optimum:

$$\begin{aligned} \mathcal{L}_n^* &= \frac{1}{2}(\delta_n^{v\dagger})^\top \mathbf{A}_n^v \delta_n^{v\dagger} + \frac{1}{2}(\delta_n^{f\dagger})^\top \mathbf{A}_n^f \delta_n^{f\dagger} \\ &\geq \frac{\lambda_{\min}(\mathbf{A}_n^v)}{2} \|\delta_n^{v\dagger}\|^2 + \frac{\lambda_{\min}(\mathbf{A}_n^f)}{2} \|\delta_n^{f\dagger}\|^2 \\ &\geq \frac{\lambda_{\min,n}}{2} (\|\delta_n^{v\dagger}\|^2 + \|\delta_n^{f\dagger}\|^2), \end{aligned} \quad (26)$$

where  $\lambda_{\min,n} = \min(\lambda_{\min}(\mathbf{A}_n^v), \lambda_{\min}(\mathbf{A}_n^f)) > 0$ .

*Step B (parallelogram identity).* For any two vectors  $a, b \in \mathbb{R}^3$ ,  $\|a\|^2 + \|b\|^2 = 2\|(a+b)/2\|^2 + \|a-b\|^2/2 \geq \|a-b\|^2/2$ . Setting  $a = \delta_n^{v\dagger}$ ,  $b = \delta_n^{f\dagger}$ , and using  $\delta_n^{v\dagger} - \delta_n^{f\dagger} = -v\Delta\tau$ :

$$\|\delta_n^{v\dagger}\|^2 + \|\delta_n^{f\dagger}\|^2 \geq \frac{\|\delta_n^{v\dagger} - \delta_n^{f\dagger}\|^2}{2} = \frac{\|v\Delta\tau\|^2}{2} = \frac{\|v\|^2 |\Delta\tau|^2}{2}. \quad (27)$$

*Combining Steps A and B* and summing over all  $N$  Gaussians:

$$\mathcal{L}_{\text{single}}^* = \sum_{n=1}^N \mathcal{L}_n^* \geq \frac{\|v\|^2 |\Delta\tau|^2}{4} \sum_{n=1}^N \lambda_{\min,n} > 0. \quad (28)$$

This completes the proof of Part (i). The bound is strict and *representation-level*: no choice of canonical parameters can reduce the photometric loss below this threshold, regardless of the optimizer used. The irreducible error scales quadratically with both the agent velocity  $\|v\|$  and the temporal offset  $|\Delta\tau|$ , and linearly with the aggregate Fisher information  $\sum_n \lambda_{\min,n}$ —all quantities that are large in typical high-speed VICAD scenarios.

The formula for the theorem 1 in the Sec 3.2 is obtained by reformulating  $\lambda_{\min,n}$  as  $\lambda_n$ .

$$\mathcal{L}_{\text{single}}^* \geq \frac{|\Delta\tau|^2 \|v\|^2}{4} \sum_{n=1}^N \lambda_n > 0, \quad (29)$$

where  $\lambda_n > 0$  is the minimum Fisher-information eigenvalue of  $\mathcal{G}_n$ , quantifying its photometric sensitivity to displacement.

## B.4 Proof of Part (ii): Gradient Incompatibility

We now show that the two per-source gradients cannot simultaneously vanish at any canonical parameter, and quantify the separation between their individual optima. From Eq. (18), the gradient of  $\mathcal{L}^c$  with respect to  $\bar{\mu}_n$

vanishes when

$$\begin{aligned}
\nabla_{\bar{\mu}_n} \mathcal{L}^c = \mathbf{0} &\iff (R_i)^\top \mathbf{A}_n^c \delta_n^c = \mathbf{0} \\
&\iff \mathbf{A}_n^c \delta_n^c = \mathbf{0} \\
&\iff \delta_n^c = \mathbf{0} \\
&\iff \mu_n = \mu_n^{*,c},
\end{aligned} \tag{30}$$

where the second equivalence uses  $R_i \in SO(3)$  (invertible) and the third uses  $\mathbf{A}_n^c \succ 0$  (invertible). Thus  $\mathcal{L}^v$  is minimized at  $\mu_n = \mu_n^{*,v}$  and  $\mathcal{L}^f$  is minimized at  $\mu_n = \mu_n^{*,f}$ .

Since  $\mu_n = R_i \bar{\mu}_n + T_i$  is a bijection in  $\bar{\mu}_n$ , the per-source canonical optima are  $\bar{\mu}_n^{*,v} = R_i^\top (\mu_n^{*,v} - T_i)$  and  $\bar{\mu}_n^{*,f} = R_i^\top (\mu_n^{*,f} - T_i)$ . Their separation is

$$\begin{aligned}
\|\bar{\mu}_n^{*,v} - \bar{\mu}_n^{*,f}\| &= \|R_i^\top (\mu_n^{*,v} - \mu_n^{*,f})\| \\
&= \|\mu_n^{*,v} - \mu_n^{*,f}\| \quad (R_i \in SO(3) \text{ is isometric}) \\
&= \|v \Delta\tau\| = \|v\| |\Delta\tau|.
\end{aligned} \tag{31}$$

Since  $v \neq \mathbf{0}$  and  $\Delta\tau \neq 0$ , this separation is strictly positive, so no single  $\bar{\mu}_n$  can simultaneously satisfy both  $\nabla_{\bar{\mu}_n} \mathcal{L}^v = \mathbf{0}$  and  $\nabla_{\bar{\mu}_n} \mathcal{L}^f = \mathbf{0}$ . The separation  $\|v\| |\Delta\tau|$  is the physical displacement of the agent between the two capture times projected into canonical space. For a vehicle traveling at  $\|v\| = 10$  m/s with  $|\Delta\tau| = 70$  ms, this equals 0.7 m—far exceeding the typical Gaussian kernel radius in driving scenes. The optimizer is forced to place  $\bar{\mu}_n$  at the Fisher-weighted compromise (Eq. (24)), creating blurred, ghosted reconstructions that satisfy neither view.

**Gradient anti-alignment in the worst case.** When  $t_i$  lies between the two capture times, i.e.,  $(\tau_v - t_i)(\tau_f - t_i) < 0$ , the positional offsets  $\delta_n^v$  and  $\delta_n^f$  at the anchor position  $\mu_n = \mu_n^*(t_i)$  point in opposite directions along  $v$ . Under the isotropic Fisher approximation  $\mathbf{A}_n^v \approx \mathbf{A}_n^f \approx \lambda_n I_3$ , the per-source gradients from Eq. (18) become

$$\begin{aligned}
\nabla_{\bar{\mu}_n} \mathcal{L}^v &\approx (R_i)^\top \mathbf{A}_n^v \delta_n^v \\
&= \lambda_n (R_i)^\top (\mu_n^*(t_i) - \mu_n^{*,v}) \\
&= \lambda_n (R_i)^\top (-v(\tau_v - t_i)) \quad [\text{from Eq. (21)}] \\
&= -\lambda_n (R_i)^\top v(\tau_v - t_i),
\end{aligned} \tag{32}$$

and analogously  $\nabla_{\bar{\mu}_n} \mathcal{L}^f \approx -\lambda_n (R_i)^\top v(\tau_f - t_i)$ . The cosine similarity between the two gradient vectors is

$$\begin{aligned}
\cos \angle(\nabla_{\bar{\mu}_n} \mathcal{L}^v, \nabla_{\bar{\mu}_n} \mathcal{L}^f) &= \frac{\nabla_{\bar{\mu}_n} \mathcal{L}^v \cdot \nabla_{\bar{\mu}_n} \mathcal{L}^f}{\|\nabla_{\bar{\mu}_n} \mathcal{L}^v\| \|\nabla_{\bar{\mu}_n} \mathcal{L}^f\|} \\
&= \frac{\lambda_n^2 \|(R_i)^\top v\|^2 (\tau_v - t_i)(\tau_f - t_i)}{\lambda_n^2 \|(R_i)^\top v\|^2 |\tau_v - t_i| |\tau_f - t_i|} \\
&= \frac{(\tau_v - t_i)(\tau_f - t_i)}{|\tau_v - t_i| |\tau_f - t_i|} = -1,
\end{aligned} \tag{33}$$

where the last equality holds because  $(\tau_v - t_i)$  and  $(\tau_f - t_i)$  have opposite signs, and  $\|(R_i)^\top v\| = \|v\| > 0$  since  $R_i \in SO(3)$  is isometric. This is the most severe form of gradient conflict: the two sources provide diametrically opposed update signals to the shared canonical parameters. Even when the anchor does not lie between the capture times, the cosine similarity satisfies

$$\cos \angle(\nabla_{\bar{\mu}_n} \mathcal{L}^v, \nabla_{\bar{\mu}_n} \mathcal{L}^f) = \frac{(\tau_v - t_i)(\tau_f - t_i)}{|\tau_v - t_i| |\tau_f - t_i|} < +1 \quad \text{whenever } \Delta\tau \neq 0, \tag{34}$$

ensuring persistent gradient interference regardless of anchor placement.  $\square$

## B.5 Proof of Part (iii): NTK Block-Diagonalization

We now show that DUST-GSG simultaneously eliminates the irreducible residual and the gradient conflict by introducing source-specific pose degrees of freedom.

Under DUST-GSG, source  $c$  uses its own pose  $P^c(\tau_c) = (R^c, T^c)$  at its actual capture time  $\tau_c$ , so the world-space position of Gaussian  $n$  is  $\mu_n^c = R^c \bar{\mu}_n + T^c$ . When the poses match the ground truth, the positional error for source  $c$  becomes

$$\begin{aligned}
\delta_n^c &= \mu_n^c - \mu_n^{*,c} \\
&= R^*(\tau_c) \bar{\mu}_n + T^*(\tau_c) - (R^*(\tau_c) \bar{\mu}_n^* + T^*(\tau_c)) \\
&= R^*(\tau_c) (\bar{\mu}_n - \bar{\mu}_n^*),
\end{aligned} \tag{35}$$

where  $\bar{\mu}_n^*$  is the true canonical position, shared by both sources since it encodes the agent’s intrinsic geometry independent of capture time. Setting  $\bar{\mu}_n = \bar{\mu}_n^*$  therefore yields  $\delta_n^c = \mathbf{0}$  for *both* sources simultaneously:

$$\bar{\mu}_n = \bar{\mu}_n^* \implies \delta_n^v = \delta_n^f = \mathbf{0} \implies \mathcal{L}_{\text{DST}}^* = \sum_{n=1}^N (\mathcal{L}_n^v + \mathcal{L}_n^f) = 0. \quad (36)$$

The key mechanism is that the source-specific poses  $P^v, P^f$  absorb the temporal discrepancy: each pose places the agent at the correct world position for its own capture time, so the canonical parameters need only encode the agent’s intrinsic shape. This is in direct contrast to the single-timeline case, where no canonical parameter can simultaneously satisfy  $\delta_n^v = \mathbf{0}$  and  $\delta_n^f = \mathbf{0}$  (Part (ii)).

To analyze the optimization dynamics, we employ the Empirical Neural Tangent Kernel (NTK) adapted to the Gaussian splatting renderer. Let  $\theta \in \mathbb{R}^d$  be the full optimizable parameter vector; the empirical NTK is the  $M \times M$  matrix with entries

$$\Theta(\mathbf{x}_k, \mathbf{x}_l) = \langle \nabla_{\theta} \hat{I}^{c_k}(u_k; \theta), \nabla_{\theta} \hat{I}^{c_l}(u_l; \theta) \rangle, \quad (37)$$

where  $\mathbf{x}_k = (u_k, c_k)$  indexes pixel  $u_k$  from source  $c_k$ . Under gradient flow on the squared loss, the residual vector  $\mathbf{r}(t) = \hat{\mathbf{I}}(t) - \mathbf{I}^*$  evolves as  $\dot{\mathbf{r}}(t) \approx -\Theta(0) \mathbf{r}(t)$  in the linearized regime (Assumption 1), so the spectral properties of  $\Theta$  govern the optimization dynamics. Partitioning the parameter vector as  $\theta = (\bar{\mu}, \xi)$ , where  $\bar{\mu} \in \mathbb{R}^{3N}$  collects the canonical means and  $\xi$  collects the pose parameters, the NTK decomposes additively:  $\Theta = \Theta^{\bar{\mu}} + \Theta^{\xi}$ .

In the single-timeline formulation, the shared pose  $\xi \in \mathbb{R}^6$  couples both sources, giving the pose Jacobian  $J_{\xi}^{\text{single}} = (\nabla_{\xi} \hat{\mathbf{I}}^v; \nabla_{\xi} \hat{\mathbf{I}}^f) \in \mathbb{R}^{M \times 6}$  and the pose kernel

$$\Theta_{\text{single}}^{\xi} = J_{\xi}^{\text{single}} (J_{\xi}^{\text{single}})^{\top} = \begin{pmatrix} \nabla_{\xi} \hat{\mathbf{I}}^v (\nabla_{\xi} \hat{\mathbf{I}}^v)^{\top} & \nabla_{\xi} \hat{\mathbf{I}}^v (\nabla_{\xi} \hat{\mathbf{I}}^f)^{\top} \\ \nabla_{\xi} \hat{\mathbf{I}}^f (\nabla_{\xi} \hat{\mathbf{I}}^v)^{\top} & \nabla_{\xi} \hat{\mathbf{I}}^f (\nabla_{\xi} \hat{\mathbf{I}}^f)^{\top} \end{pmatrix}. \quad (38)$$

The off-diagonal blocks  $\nabla_{\xi} \hat{\mathbf{I}}^v (\nabla_{\xi} \hat{\mathbf{I}}^f)^{\top}$  are generically non-zero: a pose update driven by the vehicle loss simultaneously perturbs the infrastructure residuals, and vice versa. This is the NTK-level manifestation of the gradient conflict identified in Part (ii).

Under DUST-GSG, the poses are parameterized by separate  $\xi^v \in \mathbb{R}^6$  and  $\xi^f \in \mathbb{R}^6$ . Since the vehicle renderer uses only  $P^v(\xi^v)$  and the infrastructure renderer uses only  $P^f(\xi^f)$ , there is no functional dependence between them:  $\partial \hat{I}^v(u)/\partial \xi^f = \mathbf{0}$  and  $\partial \hat{I}^f(u)/\partial \xi^v = \mathbf{0}$  for all  $u$ . The pose Jacobian therefore has a block-diagonal structure:

$$J_{\xi}^{\text{DST}} = \begin{pmatrix} \nabla_{\xi^v} \hat{\mathbf{I}}^v & \mathbf{0} \\ \mathbf{0} & \nabla_{\xi^f} \hat{\mathbf{I}}^f \end{pmatrix} \in \mathbb{R}^{M \times 12}, \quad (39)$$

and the resulting pose kernel is

$$\begin{aligned} \Theta_{\text{DST}}^{\xi} &= J_{\xi}^{\text{DST}} (J_{\xi}^{\text{DST}})^{\top} \\ &= \begin{pmatrix} \nabla_{\xi^v} \hat{\mathbf{I}}^v (\nabla_{\xi^v} \hat{\mathbf{I}}^v)^{\top} & \mathbf{0} \\ \mathbf{0} & \nabla_{\xi^f} \hat{\mathbf{I}}^f (\nabla_{\xi^f} \hat{\mathbf{I}}^f)^{\top} \end{pmatrix} \\ &= \text{diag}(\Theta_{vv}^{\xi^v}, \Theta_{ff}^{\xi^f}), \end{aligned} \quad (40)$$

where  $\Theta_{vv}^{\xi^v} := \nabla_{\xi^v} \hat{\mathbf{I}}^v (\nabla_{\xi^v} \hat{\mathbf{I}}^v)^{\top} \in \mathbb{R}^{M_v \times M_v}$  and  $\Theta_{ff}^{\xi^f} := \nabla_{\xi^f} \hat{\mathbf{I}}^f (\nabla_{\xi^f} \hat{\mathbf{I}}^f)^{\top} \in \mathbb{R}^{M_f \times M_f}$ . The off-diagonal blocks vanish identically, establishing the block-diagonal structure asserted in Eq. (40).

Partitioning the full residual vector as  $\mathbf{r}(t) = (\mathbf{r}^v(t)^{\top}, \mathbf{r}^f(t)^{\top})^{\top}$ , the gradient flow restricted to pose parameters evolves as

$$\frac{d}{dt} \begin{pmatrix} \mathbf{r}^v \\ \mathbf{r}^f \end{pmatrix} = -\Theta_{\text{DST}}^{\xi} \begin{pmatrix} \mathbf{r}^v \\ \mathbf{r}^f \end{pmatrix} = - \begin{pmatrix} \Theta_{vv}^{\xi^v} & \mathbf{0} \\ \mathbf{0} & \Theta_{ff}^{\xi^f} \end{pmatrix} \begin{pmatrix} \mathbf{r}^v \\ \mathbf{r}^f \end{pmatrix}. \quad (41)$$

The block-diagonal structure decouples the two subsystems completely:

$$\dot{\mathbf{r}}^v(t) = -\Theta_{vv}^{\xi^v} \mathbf{r}^v(t), \quad \dot{\mathbf{r}}^f(t) = -\Theta_{ff}^{\xi^f} \mathbf{r}^f(t). \quad (42)$$

These two ODEs are independent: the closed-form solution  $\mathbf{r}^v(t) = e^{-\Theta_{vv}^{\xi^v} t} \mathbf{r}^v(0)$  depends only on  $\xi^v$  and  $\mathbf{r}^v(0)$ , with no dependence on  $\xi^f$  or  $\mathbf{r}^f$ , and vice versa. Consequently, a gradient step on  $\xi^v$  driven by  $\mathbf{r}^v$  produces *exactly zero* change in  $\mathbf{r}^f$ , and vice versa—the precise sense in which DUST-GSG eliminates cross-source gradient interference at the pose level. Combined with the zero-residual result of Eq. (36), this establishes all three claims of Part (iii).  $\square$

## C Implementation Details

### C.1 Initialization

For the background model, we combine  $8 \times 10^5$  LiDAR points with  $2 \times 10^5$  random samples, divided into  $1 \times 10^5$  near samples uniformly distributed by distance to the scene’s origin and  $1 \times 10^5$  far samples uniformly distributed by inverse distance. We filter out LiDAR samples belonging to dynamic objects. For rigid nodes and non-rigid deformable nodes, we utilize their tracking bounding boxes to accumulate LiDAR points. Each dynamic instance is initialized with at most 5 000 canonical Gaussians, and we only model moving instances, with trajectory length thresholds of 1.0 for rigid nodes and 0.5 for deformable nodes. To determine the initial color, LiDAR points are projected onto the image plane, whereas random samples are initialized with random colors.

Prior to training, we perform offline Pose Correction to initialize the dual-timeline poses. Co-visible static vehicles serve as geometric anchors, matched across the vehicle and infrastructure views Euclidean distance and the Hungarian method. A 6-DoF pose correction is estimated by minimizing corner alignment error using L-BFGS. The refined poses regenerate cooperative labels, and missing tracks are filled via linear interpolation for translation and Slerp for rotation for gaps up to two frames. These labels initialize separate pose trajectories for the vehicle-side and infrastructure-side timelines, with all timestamps normalized to  $[0, 1]$ .

### C.2 Training

Our method trains for 30 000 iterations with all scene nodes optimized jointly. The learning rate for background Gaussian properties aligns with the default settings of 3DGS: positions at  $1.6 \times 10^{-4}$  (decaying to  $1.6 \times 10^{-6}$ ), SH DC at  $2.5 \times 10^{-3}$ , SH rest at  $1.25 \times 10^{-4}$ , opacity at  $5 \times 10^{-2}$ , scaling at  $5 \times 10^{-3}$ , and rotation at  $1 \times 10^{-3}$ . The degrees of spherical harmonics are reset to 3 for background nodes, rigid nodes, and deformable nodes. For deformable nodes, the canonical position learning rate is scaled by a factor of 2.0.

The learning rate for the rotation of instance poses is  $1 \times 10^{-5}$ , decreasing exponentially to  $5 \times 10^{-6}$ . The learning rate for the translation of instance poses is  $5 \times 10^{-4}$ , decreasing exponentially to  $1 \times 10^{-4}$ . For deformable nodes, the deformation network (8 layers, 256 channels) uses a learning rate of  $1.6 \times 10^{-3}$ , decaying to  $1.6 \times 10^{-4}$ , and the temporal embedding uses  $1 \times 10^{-3}$ , decaying to  $1 \times 10^{-4}$ . The sky environment map is optimized at 0.01. Affine transformation and camera pose refinement modules both use  $1 \times 10^{-5}$ .

For the Gaussian densification strategy, we utilize the absolute gradient of Gaussians. We set the densification threshold of the position gradient to  $5 \times 10^{-4}$  and the densification size threshold to  $3 \times 10^{-3}$ . We reset the opacity of Gaussians to 0.01 every 3 000 iterations, with an opacity warm-up of 500 steps and refinement every 100 steps. We stop splitting background Gaussians at 15 000 steps, rigid nodes at 30 000 steps, and deformable nodes at 20 000 steps.

The photometric loss combines L1 and SSIM with weights 0.8 and 0.2. Additional regularization includes mask (0.05), depth (0.01), affine ( $1 \times 10^{-5}$ ), and dynamic region loss (0.05, with 0.1 for vehicles and 0.05 for humans, activated from iteration 3 000). For pose regularization, temporal smoothness uses 0.01 over 5 frames; effective-translational temporal smoothness uses 0.002 over 1 frame; time-offset velocity loss is 0.01; filled residual loss is 0.02; and group residual loss is 0.01 (stopped after 12 000 steps). The drift loss weight linearly decays to zero during training.

The training process commences from a 1/4 image resolution, doubling every 250 iterations. We supervise with two asynchronous cameras (vehicle-side cam0 and roadside cam1), using independently provided timestamp files, with the roadside view as the reference for pose-group alignment. The sky environment map resolution is 1024.

Our method runs on NVIDIA A100 Tensor Core GPU, with training for each scene taking about one hour. Training time varies with different training settings.

### C.3 Optimization

Since our newly constructed regularization term for pose optimization has already been introduced in Sec 3.3, only the remaining regularization terms are detailed here. Specifically, following the implementation of OMNIRE [3], they are defined as follows:

We utilize the loss function introduced in Eq 43 to jointly optimize all learnable parameters. The image loss is computed as:

$$\mathcal{L}_{\text{image}} = (1 - \lambda_r)\mathcal{L}_1 + \lambda_r\mathcal{L}_{\text{SSIM}} \quad (43)$$

due to sparse temporal-spatial observation of the dynamic part, its supervision signal is insufficient. To address this, we apply a higher image loss weight to the dynamic regions identified by the rendered dynamic mask. This

weight is set to 5. The depth map loss is computed as:

$$\mathcal{L}_{\text{depth}} = \frac{1}{hw} \sum \left\| \mathcal{D}^s - \hat{\mathcal{D}} \right\|_1 \quad (44)$$

where  $\mathcal{D}^s$  is the inverse of the sparse depth map. We project LiDAR points onto the image plane to generate the sparse LiDAR map, and  $\hat{\mathcal{D}}$  is the inverse of the predicted depth map.

The mask loss  $\mathcal{L}_{\text{opacity}}$  is computed as:

$$\mathcal{L}_{\text{opacity}} = -\frac{1}{hw} \sum O_g \cdot \log O_g - \frac{1}{hw} \sum M_{\text{sky}} \cdot \log(1 - O_g) \quad (45)$$

where  $M_{\text{sky}}$  is the sky mask, and  $O_g$  is the rendered opacity map.

In addition to the reconstruction losses, we introduce various regularization terms for different Gaussian representations to improve quality. Among these, an important regularization term is  $\mathcal{L}_{\text{pose}}$ , designed to ensure smooth human body poses  $\theta(t)$ . This term is defined as:

$$\mathcal{L}_{\text{reg}} = \frac{1}{2} \left\| \theta(t - \delta) + \theta(t + \delta) - 2\theta(t) \right\|_1 \quad (46)$$

where  $\delta$  is a randomly chosen integer from  $\{1, 2, 3, 4, 5\}$ . We set the weight of the SSIM loss,  $\lambda_r$ , to 0.2, the depth loss,  $\lambda_{\text{depth}}$ , to 0.01, the opacity loss,  $\lambda_{\text{opacity}}$ , to 0.05, and the pose smoothness loss,  $\lambda_{\text{reg}}$ , to 0.01.

## D Evaluation

### D.1 Datasets

We evaluate our method on 26 diverse sequences selected from the large-scale V2X-Seq dataset. These sequences cover various times of data, weather and traffic densities. Specifically, for the "times of data" category, night-time V2I scenarios are not provided in the V2X-Seq [31] dataset. Thus, the period from 11:30 to 12:30 is defined as "Noon". The period from 16:30 to 17:30 is defined as "Dusk". Four sequences are selected for each time period. For the "Weather" category, only normal and rainy conditions are available in the dataset. Therefore, two subcategories are defined: "Normal" and "Rainy". Six sequences are allocated to each subcategory. For the "traffic densities" category, referred to as "Crowd", the number of agents in each sequence was counted. A higher number of agents indicates higher traffic densities. The 6 sequences with the most agents are selected as "High". The 6 sequences with the fewest agents are selected as "Low". The selected sequence id, average frames, average agent counts, and data formats for each category are detailed in Tables 4. Examples for each category are illustrated in Fig 6.

Table 4: Detailed descriptions of the sequences selected for classification are provided. The specific condition of the sequences is denoted by Cond. The average number of image frames across all sequences under each condition is represented by Frames. The average number of agents in all sequences under each condition is indicated by Agent.

Cond.	Sequence ID	Frames	Agent	Data Format
Noon	70,71,72,73	181	27	Image, LiDAR, Bounding Box
Dusk	55,56,57,58	204	22	Image, LiDAR, Bounding Box
Normal	21,23,29,30,60,63	176	17	Image, LiDAR, Bounding Box
Rainy	36,40,41,42,47,48	166	10	Image, LiDAR, Bounding Box
Low	7,21,23,36,42,79	156	5	Image, LiDAR, Bounding Box
High	2,4,59,66,71,73	240	48	Image, LiDAR, Bounding Box

### D.2 Metrics

We assess reconstruction quality using five metrics: PSNR [19], SSIM, LPIPS [33], FVD [18], and RAFT-EPE [17]. For the image-based metrics (PSNR, SSIM, and LPIPS), we report results on the full image as well as within dynamic regions. For temporal consistency, FVD and RAFT-EPE are computed exclusively within dynamic masks to avoid static back grounds dominating the motion-related evaluation.

**PSNR.** The Peak Signal-to-Noise Ratio measures pixel-wise reconstruction fidelity between the rendered image  $\hat{\mathbf{I}}$  and the ground-truth image  $\mathbf{I}$ . It is defined as:

$$\text{PSNR} = -10 \log_{10} \left( \frac{1}{N} \sum_{i=1}^N (\hat{I}_i - I_i)^2 \right), \quad (47)$$

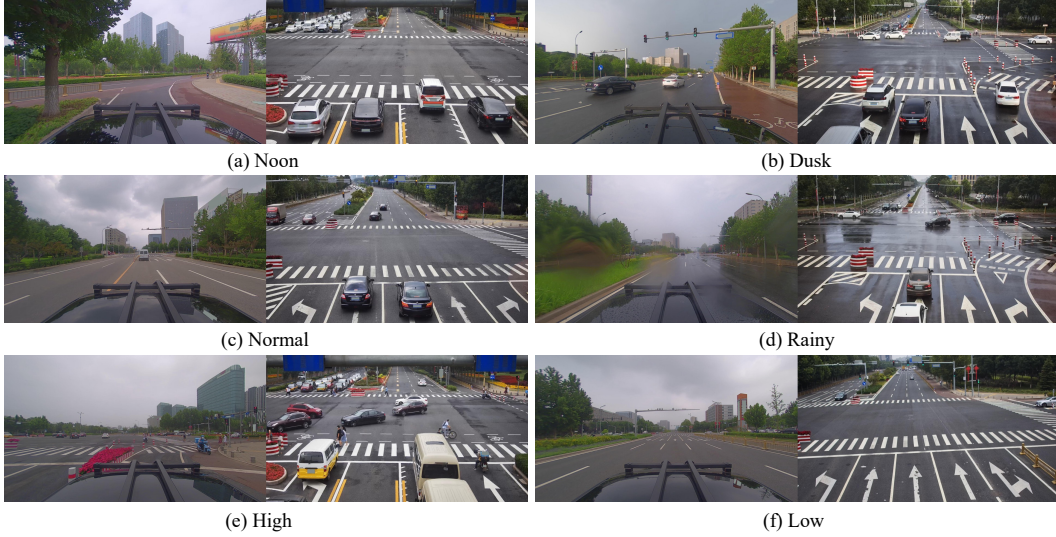


Figure 6: The images from both the vehicle and infrastructure perspectives of the dataset are presented under each condition.

where  $N$  is the number of valid pixels and pixel intensities are normalized to  $[0, 1]$ . A higher PSNR indicates lower reconstruction error.

**SSIM.** The Structural Similarity Index Measure evaluates local structural consistency by comparing luminance, contrast, and structure within a sliding Gaussian window. For two image patches  $\mathbf{x}$  and  $\mathbf{y}$ , it is formulated as:

$$\text{SSIM}(\mathbf{x}, \mathbf{y}) = \frac{(2\mu_x\mu_y + c_1)(2\sigma_{xy} + c_2)}{(\mu_x^2 + \mu_y^2 + c_1)(\sigma_x^2 + \sigma_y^2 + c_2)}, \quad (48)$$

where  $\mu_x, \mu_y$  and  $\sigma_x, \sigma_y$  are the local means and standard deviations,  $\sigma_{xy}$  is the cross-covariance, and  $c_1, c_2$  are small constants for numerical stability. We compute the full SSIM map using an  $11 \times 11$  Gaussian window and average the values over the valid pixel region.

**LPIPS.** The Learned Perceptual Image Patch Similarity measures perceptual distance using deep network features. Given rendered and ground-truth images, we extract multi-scale features from a pre-trained AlexNet and compute a normalized  $\ell_2$  distance:

$$\text{LPIPS}(\hat{\mathbf{I}}, \mathbf{I}) = \sum_{\ell} \frac{1}{H_{\ell}W_{\ell}} \sum_{h,w} \|\mathbf{w}_{\ell} \odot (\phi_{\ell}(\hat{\mathbf{I}})_{h,w} - \phi_{\ell}(\mathbf{I})_{h,w})\|_2^2, \quad (49)$$

where  $\phi_{\ell}(\cdot)$  denotes the feature map from layer  $\ell$  of the network,  $\mathbf{w}_{\ell}$  are learned channel-wise weights, and  $H_{\ell}, W_{\ell}$  are the spatial dimensions of the feature map. The input images are normalized from  $[0, 1]$  to  $[-1, 1]$  before feature extraction. Lower LPIPS indicates better perceptual similarity.

**FVD.** The Fréchet Video Distance measures temporal consistency by computing the Fréchet distance between the feature distributions of rendered and ground-truth videos. We extract spatio-temporal features using a pre-trained I3D network (trained on Kinetics) that yields 400-dimensional embeddings. For a video with  $T$  frames, we build non-overlapping clips of length  $T_c = 16$  frames. Each clip is pre-processed by resizing the shorter side to 224 pixels, center-cropping to  $224 \times 224$ , and normalizing to  $[-1, 1]$ . Let  $(\boldsymbol{\mu}_{\text{gen}}, \boldsymbol{\Sigma}_{\text{gen}})$  and  $(\boldsymbol{\mu}_{\text{real}}, \boldsymbol{\Sigma}_{\text{real}})$  denote the mean and covariance of the generated and real clip features, respectively. The FVD is defined as:

$$\text{FVD} = \|\boldsymbol{\mu}_{\text{gen}} - \boldsymbol{\mu}_{\text{real}}\|_2^2 + \text{Tr}\left(\boldsymbol{\Sigma}_{\text{gen}} + \boldsymbol{\Sigma}_{\text{real}} - 2\sqrt{\boldsymbol{\Sigma}_{\text{gen}}\boldsymbol{\Sigma}_{\text{real}}}\right), \quad (50)$$

where  $\text{Tr}(\cdot)$  is the matrix trace and  $\sqrt{\cdot}$  denotes the matrix square root. Following standard practice, FVD is computed only within dynamic regions so that temporal consistency of moving agents is emphasized.

**RAFT-EPE.** To evaluate motion plausibility, we compute the End-Point Error (EPE) between optical flows estimated from consecutive rendered frames and the corresponding ground-truth frames. We use RAFT with the pre-trained weights on FlyingThings (raft-things.pth) and run inference with 20 update iterations. For consecutive frames  $\mathbf{I}_t$  and  $\mathbf{I}_{t+1}$ , RAFT predicts a dense flow field  $\mathbf{F}_t \in \mathbb{R}^{H \times W \times 2}$  with horizontal and vertical components  $(u, v)$ . The EPE is computed as:

$$\text{EPE} = \frac{1}{|\mathcal{M}|} \sum_{(h,w) \in \mathcal{M}} \sqrt{(\hat{u}_{h,w} - u_{h,w})^2 + (\hat{v}_{h,w} - v_{h,w})^2}, \quad (51)$$

where  $\mathcal{M}$  denotes the union of dynamic masks from both frames, ensuring evaluation focuses strictly on moving regions.

### D.3 Baselines

To evaluate the effectiveness of our approach, our method is compared with several state-of-the-art baselines.

- **3DGS [7]**: 3D Gaussian Splatting (3DGS) is utilized for real-time and high-quality novel-view synthesis. Continuous volumetric radiance fields are represented by 3D Gaussians. These Gaussians are initialized from sparse calibration points. Interleaved optimization and density control are performed to accurately represent the scene geometry. A fast visibility-aware rendering algorithm is developed to support anisotropic splatting and real-time rendering.
- **PVG [2]**: Periodic Vibration Gaussian (PVG) is introduced to model dynamic urban scenes. A unified representation model is presented to capture the synergistic interactions of static and dynamic elements. Periodic vibration-based temporal dynamics are incorporated into the 3D Gaussian splatting technique. To handle sparse training data, a temporal smoothing mechanism and a position-aware adaptive control strategy are proposed. High-quality reconstruction is achieved without manually labeled bounding boxes or optical flow estimation.
- **OMNIRE [3]**: OMNIRE is presented as a comprehensive system for the creation of high-fidelity digital twins from on-device logs. Diverse dynamic objects, including vehicles and pedestrians, are fully reconstructed. Scene graphs are built on 3DGS. Multiple Gaussian representations are constructed in canonical spaces to model various dynamic actors. Advanced simulations with human-participated scenarios are supported by this holistic reconstruction capability.
- **CRUISE [22]**: CRUISE is proposed as a comprehensive reconstruction and synthesis framework for Vehicle-to-everything (V2X) driving environments. Real-world scenes are accurately reconstructed using decomposed Gaussian Splatting. Dynamic traffic participants are decomposed into editable Gaussian representations. Images from both ego-vehicle and infrastructure views are rendered to facilitate large-scale V2X dataset augmentation.
- **StreetGS [26]**: Street Gaussians (StreetGS) is introduced to model dynamic urban streets. The dynamic urban scene is explicitly represented as a set of point clouds equipped with semantic logits and 3D Gaussians. Foreground vehicles and the background are modeled separately. Tracked poses and a 4D spherical harmonics model are optimized to capture the dynamics and appearance of object vehicles. Fast scene editing and rendering are achieved by this explicit representation.
- **DeformableGS [29]**: Deformable 3D Gaussians Splatting (DeformableGS) is proposed to model monocular dynamic scenes. 3D Gaussians are learned in a canonical space. A deformation field is applied to capture the intricate details of moving objects. An annealing smoothing training mechanism is introduced to mitigate the impact of inaccurate poses. Real-time rendering and high visual quality are achieved through a differential Gaussian rasterizer.